



# **NAVAL POSTGRADUATE SCHOOL**

**MONTEREY, CALIFORNIA**

## **THESIS**

**AUTOMATED MANEUVER DESIGN AND CHECKOUT  
FOR THE LUNAR RECONNAISSANCE ORBITER**

by

James M. Kaufman

December 2014

Thesis Advisor:

Co-Advisor:

Mark Karpenko

I. Michael Ross

**Approved for public release; distribution is unlimited**

THIS PAGE INTENTIONALLY LEFT BLANK

REPORT DOCUMENTATION PAGE			Form Approved OMB No. 0704-0188	
Public reporting burden for this collection of information is estimated to average 1 hour per response, including the time for reviewing instruction, searching existing data sources, gathering and maintaining the data needed, and completing and reviewing the collection of information. Send comments regarding this burden estimate or any other aspect of this collection of information, including suggestions for reducing this burden, to Washington headquarters Services, Directorate for Information Operations and Reports, 1215 Jefferson Davis Highway, Suite 1204, Arlington, VA 22202-4302, and to the Office of Management and Budget, Paperwork Reduction Project (0704-0188) Washington, DC 20503.				
1. AGENCY USE ONLY (Leave blank)		2. REPORT DATE December 2014	3. REPORT TYPE AND DATES COVERED Master's Thesis	
4. TITLE AND SUBTITLE AUTOMATED MANEUVER DESIGN AND CHECKOUT FOR THE LUNAR RECONNAISSANCE ORBITER			5. FUNDING NUMBERS	
6. AUTHOR(S) James M. Kaufman				
7. PERFORMING ORGANIZATION NAME(S) AND ADDRESS(ES) Naval Postgraduate School Monterey, CA 93943-5000			8. PERFORMING ORGANIZATION REPORT NUMBER	
9. SPONSORING /MONITORING AGENCY NAME(S) AND ADDRESS(ES)			10. SPONSORING/MONITORING AGENCY REPORT NUMBER	
11. SUPPLEMENTARY NOTES The views expressed in this thesis are those of the author and do not reflect the official policy or position of the Department of Defense or the U.S. Government. IRB protocol number ____ N/A ____.				
12a. DISTRIBUTION / AVAILABILITY STATEMENT Approved for public release; distribution is unlimited			12b. DISTRIBUTION CODE A	
13. ABSTRACT (maximum 200 words)  The Lunar Reconnaissance Orbiter (LRO) is a lunar surface mapping and data collection mission launched by NASA in 2009. As a mapping and imaging mission, frequent attitude maneuvering is required. The LRO currently follows a trial-and-error method to design maneuvers to prevent sensitive instruments from pointing at bright objects that may damage the equipment. Additionally, eigenaxis maneuvers are the primary method by which the attitude is controlled.  In this thesis, optimal control theory is applied to provide automated maneuver design capabilities to support the LRO mission. The approach allows dynamic constraints, as well as other constraints such as occultation avoidance, to be easily incorporated into the maneuver design process. This aspect also simplifies maneuver checkout activities. The results of this thesis show that maneuvers can be designed to reorient the LRO in the presence of multiple occultation constraints. Moreover, maneuver times can be reduced up to 90 percent compared to the conventional approach. This increases the potential for efficient science data collection.				
14. SUBJECT TERMS optimal control, Lunar Reconnaissance Orbiter, LRO, attitude maneuver, occultation avoidance			15. NUMBER OF PAGES 95	
			16. PRICE CODE	
17. SECURITY CLASSIFICATION OF REPORT Unclassified	18. SECURITY CLASSIFICATION OF THIS PAGE Unclassified	19. SECURITY CLASSIFICATION OF ABSTRACT Unclassified	20. LIMITATION OF ABSTRACT UU	

NSN 7540-01-280-5500

Standard Form 298 (Rev. 2-89)  
Prescribed by ANSI Std. Z39-18

THIS PAGE INTENTIONALLY LEFT BLANK

**Approved for public release; distribution is unlimited**

**AUTOMATED MANEUVER DESIGN AND CHECKOUT FOR THE LUNAR  
RECONNAISSANCE ORBITER**

James M. Kaufman  
Lieutenant, United States Navy  
B.S., University of Washington, 2007

Submitted in partial fulfillment of the  
requirements for the degree of

**MASTER OF SCIENCE IN ASTRONAUTICAL ENGINEERING**

from the

**NAVAL POSTGRADUATE SCHOOL  
December 2014**

Author: James M. Kaufman

Approved by: Mark Karpenko  
Thesis Advisor

I. Michael Ross  
Co-Advisor

Garth V. Hobson  
Chair, Department of Mechanical and Aerospace  
Engineering

THIS PAGE INTENTIONALLY LEFT BLANK

## **ABSTRACT**

The Lunar Reconnaissance Orbiter (LRO) is a lunar surface mapping and data collection mission launched by NASA in 2009. As a mapping and imaging mission, frequent attitude maneuvering is required. The LRO currently follows a trial-and-error method to design maneuvers to prevent sensitive instruments from pointing at bright objects that may damage the equipment. Additionally, eigenaxis maneuvers are the primary method by which the attitude is controlled.

In this thesis, optimal control theory is applied to provide automated maneuver design capabilities to support the LRO mission. The approach allows dynamic constraints, as well as other constraints such as occultation avoidance, to be easily incorporated into the maneuver design process. This aspect also simplifies maneuver checkout activities. The results of this thesis show that maneuvers can be designed to reorient the LRO in the presence of multiple occultation constraints. Moreover, maneuver times can be reduced up to 90 percent compared to the conventional approach. This increases the potential for efficient science data collection.

THIS PAGE INTENTIONALLY LEFT BLANK



## TABLE OF CONTENTS

I.	INTRODUCTION AND BACKGROUND.....	1
A.	LUNAR RECONNAISSANCE ORBITER.....	1
B.	OPTIMAL CONTROL THEORY.....	4
II.	LUNAR RECONNAISSANCE ORBITER DYNAMIC MODEL.....	11
III.	RECONSTRUCTION OF EXISTING SLEW ALGORITHM.....	15
A.	BASELINE MANEUVER PERFORMANCE.....	18
IV.	AUTOMATED MANEUVER DESIGN AND CHECKOUT .....	23
A.	OPTIMAL CONTROL PROBLEM.....	23
1.	Necessary Conditions .....	24
B.	MANEUVER CHECKOUT METHODOLOGY .....	28
C.	INITIAL RESULTS .....	29
D.	MODIFICATIONS TO OPTIMAL CONTROL PROBLEM .....	34
1.	Scaling.....	34
2.	Angular Velocity Limit.....	39
V.	SUN AVOIDANCE MANEUVERS FOR LRO .....	43
A.	CASE 1: ZERO INITIAL MOMENTUM IN ALL WHEELS.....	43
1.	Poor Scaling Example .....	46
B.	CASE 2: MOMENTUM BIASED CONDITION .....	47
C.	CASE 3: ZERO NET MOMENTUM WITH MOMENTUM STORED IN INDIVIDUAL WHEELS .....	52
1.	Case 3 with Final Momentum Unspecified .....	53
2.	Case 3 with Final Momentum Specified.....	58
D.	CASE 4: MANEUVERS WITH ADDITIONAL OCCULTATION AVOIDANCE CONSTRAINTS .....	61
E.	MANEUVER CHECKOUT.....	67
VI.	CONCLUSIONS AND FUTURE WORK .....	73
	LIST OF REFERENCES.....	75
	INITIAL DISTRIBUTION LIST .....	77

THIS PAGE INTENTIONALLY LEFT BLANK

## LIST OF FIGURES

Figure 1.	The LRO and instruments, after [2].	3
Figure 2.	Illustration of sun avoidance angle calculation.	14
Figure 3.	Direct slew and dogleg maneuver.	17
Figure 4.	Angular proximity of +z axis to center of sun avoidance cone.	17
Figure 5.	Process of locating $\hat{C}$ .	20
Figure 6.	Simulink propagator used for maneuver checkout.	29
Figure 7.	S/C orientation evolution for initial problem formulation.	30
Figure 8.	Angle between S/C +z axis and sun vector for initial problem formulation.	30
Figure 9.	S/C angular velocity evolution for initial problem formulation.	31
Figure 10.	RW momentum storage for initial problem formulation.	31
Figure 11.	Control signals for initial problem formulation.	32
Figure 12.	Switching function for first control for initial problem formulation.	34
Figure 13.	Rate costates for initial problem formulation.	35
Figure 14.	Hamiltonian for the poorly scaled problem formulation.	36
Figure 15.	Initial problem formulation: S/C angular velocities for scaled problem.	38
Figure 16.	Initial problem formulation: rate costates for scaled problem.	39
Figure 17.	Initial problem formulation: Hamiltonian for scaled problem.	39
Figure 18.	S/C attitude evolution for case 1.	44
Figure 19.	Angle between S/C +z axis and sun vector for case 1.	44
Figure 20.	Control signals for case 1.	45
Figure 21.	RW momenta for case 1.	45
Figure 22.	S/C angular rates for case 1.	46
Figure 23.	S/C attitude evolution for poorly scaled case 1.	47
Figure 24.	S/C attitude evolution for case 2.2.	49
Figure 25.	Angle between S/C +z axis and sun vector for case 2.2.	49
Figure 26.	Ratio of $\omega \times (J\omega + Zr_{\max})$ to $Z\tau_{\max}$ as a function of $r$ , with $\omega = [0.5, 0.5, 0.5]^T$ .	50
Figure 27.	S/C angular rates for case 2.2.	51
Figure 28.	RW momenta for case 2.2.	51
Figure 29.	S/C attitude evolution for case 2.3.	52
Figure 30.	S/C attitude evolution for case 3.2.	54
Figure 31.	Angle between S/C +z axis and sun vector for case 3.2.	54
Figure 32.	S/C angular rates for case 3.2.	55
Figure 33.	RW momenta for case 3.2.	55
Figure 34.	S/C attitude evolution for case 3.7.	56
Figure 35.	Angle between S/C +z axis and sun vector for case 3.7.	57
Figure 36.	RW momenta for case 3.7.	58
Figure 37.	S/C orientation evolution for case 3.2a.	59
Figure 38.	Angle between S/C +z axis and sun vector for case 3.2a.	60

Figure 39.	RW momenta for case 3.2a.....	61
Figure 40.	Constraint violations using the path solved for case 3.2.....	62
Figure 41.	Angle between S/C +x axis and Earth vector for case 3.2.....	63
Figure 42.	Angle between S/C +y axis and sun vector for case 3.2. ....	63
Figure 43.	S/C orientation evolution for case 4.....	64
Figure 44.	Angle between S/C +z axis and sun vector for case 4 .....	64
Figure 45.	Angle between S/C +x axis and Earth vector for case 4.....	65
Figure 46.	Angle between S/C +y axis and sun vector for case 4 .....	65
Figure 47.	S/C angular velocities for case 4. ....	66
Figure 48.	RW momenta for case 4.....	66
Figure 49.	Checkout of the quaternion norm for case 4.....	67
Figure 50.	Checkout of the Hamiltonian for case 4.....	68
Figure 51.	Checkout of the momentum costates for case 4. ....	69
Figure 52.	Attitude checkout for case 4. ....	70
Figure 53.	Angular rate checkout for case 4.....	70
Figure 54.	RW momentum checkout for case 4.....	71
Figure 55.	Standoff angles checkout for case 4.....	71

## LIST OF TABLES

Table 1.	LRO properties and constraints, after [3] and [5].	12
Table 2.	Boundary conditions for example sun avoidance maneuver.	16
Table 3.	Estimates of status quo maneuver times.	21
Table 4.	Scaling factors for initial problem formulation.	37
Table 5.	Summary of initial momentum storage values for case 2.	48
Table 6.	Summary of initial momentum storage values for case 3.	53

THIS PAGE INTENTIONALLY LEFT BLANK

## LIST OF ACRONYMS AND ABBREVIATIONS

CRaTER	cosmic ray telescope for the effects of radiation
DCM	direction cosine matrix
DLRE	diviner lunar radiometer experiment
EOL	end of life
ISS	International Space Station
LAMP	Lyman alpha mapping project
LEND	lunar exploration neutron detector
LOLA	lunar orbiter laser altimeter
LRO	Lunar Reconnaissance Orbiter
LROC	Lunar Reconnaissance Orbiter camera
Mini-RF	miniature radio frequency
NASA	National Aeronautics and Space Administration
PDS	Planetary Data System
S/C	spacecraft
TRACE	Transition Region And Coronal Explorer
UV	ultraviolet
V&V	validation and verification

THIS PAGE INTENTIONALLY LEFT BLANK



## ACKNOWLEDGMENTS

I would like to thank the following people:

Dr. Mark Karpenko and Dr. Mike Ross, for your extensive support throughout the thesis writing process. Without your expertise and liaising with the people over at LRO, this thesis would not have even started, much less been completed. I have learned a great deal from the two of you.

CAPT Steve Frick, Dr. Jim Newman, and CAPT Dan Bursch, the former astronauts on the NPS staff, for rekindling my childhood dream of becoming an astronaut. I hope to someday be fortunate enough to join your exclusive club, educate and inspire the public, and to further our understanding of our tiny corner of the universe.

Dr. Jennifer Rhatigan and Mr. Dan Sakoda for your help with non-thesis projects. I appreciate your willingness to entertain my repeated elementary questions, not to mention that I learned a lot in your classes.

RADM Jerry Ellis for your mentorship throughout my work with the Naval Submarine League. I may have done my research on space systems, but I am first and foremost a submariner and am honored to have you as a mentor.

Dr. Bong Wie, for writing such an excellent book on spacecraft dynamics. The textbook saved me on multiple occasions and I am sure will continue to do so.

My beloved wife, Monika, for putting up with me sitting in front of my computer late on weekends to do research or writing. Also, thank you to my pets Tetra, Dante, Pickles, and Tortellini for maintaining my sanity by distracting me from time to time, perhaps a little too often. Way too often.

Lastly, thank you to the guys I worked with for 27 months in the 591 curriculum here at the Naval Postgraduate School. It has been a great pleasure and I learned a lot from each and every one of you. Fair winds and following seas, and I hope to serve with you once again in the future.

THIS PAGE INTENTIONALLY LEFT BLANK

## **I. INTRODUCTION AND BACKGROUND**

As computer technology improves, new tools are continuously becoming available to perform complex calculations for design, simulation, and operation. One field which has largely remained unchanged despite these advances is control theory. In control theory, handling additional complexity often requires large matrix operations or iterative calculations, something which was not feasible before low power, high throughput computers. In the field of control theory, particularly in control of space systems, implementation of new technology has been slow, and control theory has tended towards those “things that work” [1]. Optimal control theory introduces a way to leverage these newly available tools to design and implement seemingly counterintuitive operations which are not viable using traditional methods, yet may improve performance with respect to various cost metrics.

This objective of this thesis is to explore the application of optimal control theory to the Lunar Reconnaissance Orbiter (LRO). Specifically, the automation of attitude maneuver design and checkout involving a real spacecraft (S/C) is examined, using the framework of optimal control, wherein optimality is viewed as a side benefit but not necessarily a requirement.

### **A. LUNAR RECONNAISSANCE ORBITER**

The Lunar Reconnaissance Orbiter (LRO) is a National Aeronautics and Space Administration (NASA) mission launched on June 18, 2009. Its primary, one year mission was lunar data collection to include temperature mapping, color imaging, and ultraviolet (UV) albedo values [1]. At the conclusion of the initial mission, the LRO’s mission was extended to continue various science objectives. These datasets are made publicly available in the Planetary Data System (PDS) [2]. The collection of data by the LRO paves the way for future lunar mission planning by NASA and others, including manned missions [1].

The LRO payload consists of 7 instruments [1, 2]:

- The cosmic ray telescope for the effects of radiation (CRaTER), which characterizes the lunar radiation environment and seeks to measure radiation effects on a mock human tissue.
- The diviner lunar radiometer experiment (DLRE), which maps surface and subsurface temperatures of the moon, looking for potential landing hazards for future missions.
- The Lyman alpha mapping project (LAMP), which seeks to discover water ice in permanently shadowed areas.
- The lunar exploration neutron detector (LEND), which is used to gather information on the neutron radiation environment and to analyze for evidence of water ice.
- The lunar orbiter laser altimeter (LOLA), which generates a high resolution, three dimensional surface map of the moon. It also identifies permanently shadowed or illuminated surfaces.
- The Lunar Reconnaissance Orbiter camera (LROC), which is a black and white surface imager with a resolution as high as one meter. A color camera at 100 meter resolution is also part of the suite.
- The miniature radio frequency (Mini-RF) searches polar regions for water ice using radar, and acts as a demonstration of concept for communication with Earth based ground stations.

A photograph of the LRO, while still in development, is shown in Figure 1. All instruments with the exception of the Mini-RF have been installed and are labeled.

To conduct maneuvers, the LRO uses four reaction wheels (RW) arranged in a tetrahedral configuration [3]. By using RWs as the primary source of torque, fuel only needs to be used for momentum dumping purposes. Momentum accumulation in the RWs in a lunar orbit is primarily due to gravity gradient effects [4]. The moon's gravitational field is less uniform than the Earth's, and thus has a large effect on spacecraft (S/C) orbiting the moon.

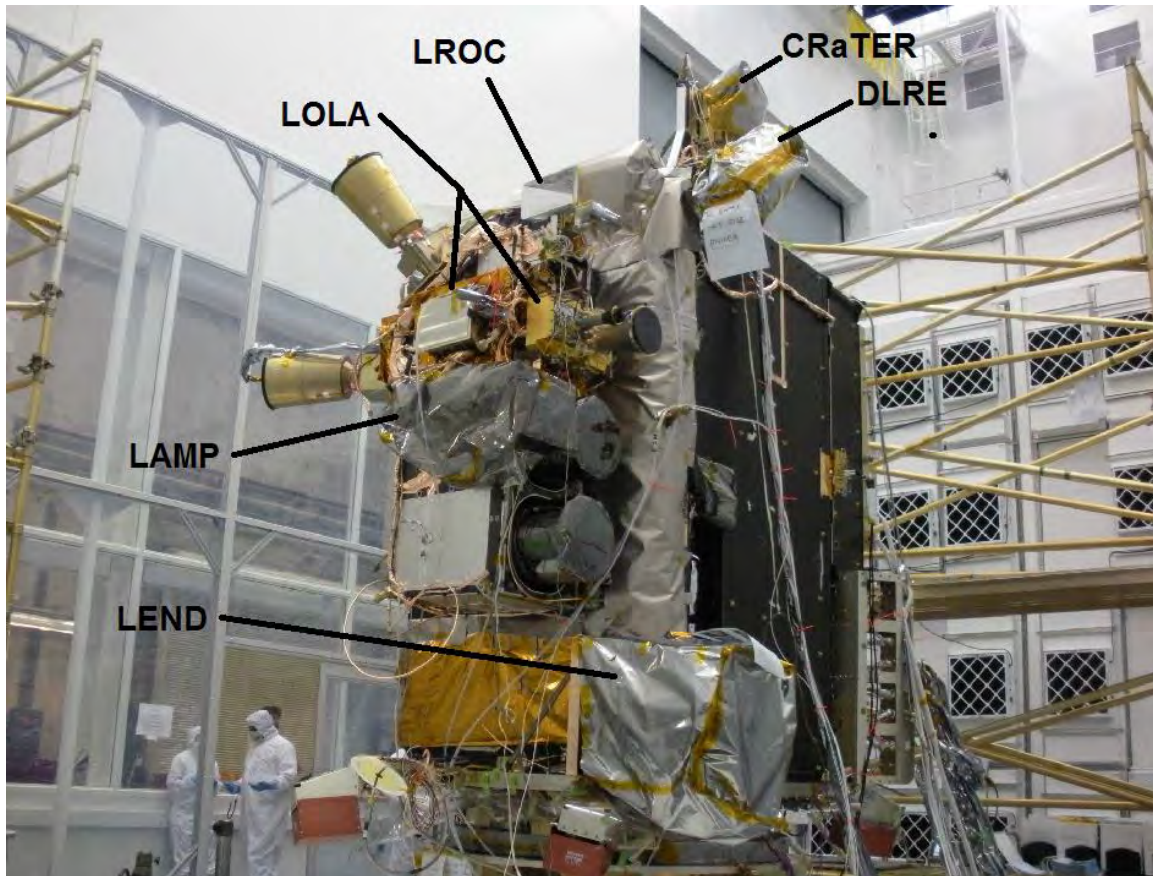


Figure 1. The LRO and instruments, after [2].

Many of LROs instrumentation and sensors are optical, such as the LROC or the star trackers used for attitude determination. These instruments are sensitive to light input, and could be damaged if exposed to a bright source such as the sun. The mapping instruments are ostensibly primarily nadir pointing, and do not usually need to worry about light from the sun. However, it is possible that when a maneuver of the S/C is required, sensitive instruments may be caused to point at or near the sun during the maneuver. This drives the need to design maneuvers in a way that prevents such damage to instruments, referred to as occultation avoidance or obstacle avoidance. Since obstacle avoidance for the LRO is done using a trial and error type approach [5], maneuver design is not autonomous; that is, that maneuver design must be done with humans in the loop. This motivates the desire to automate maneuver design [6].

Now in an extended mission, the LRO continues to collect science data. In its first five years, the LRO has collected “as much data as all other planetary missions combined” [7]. The mission has been successful, and aims to continue in its legacy to better our understanding of our closest neighbor. By implementing automated optimal maneuver design, more of the focus can shift from maneuver design to the needs of the science mission. This would simplify ground operations and increase the speed and volume of science collection.

## B. OPTIMAL CONTROL THEORY

Control theory refers to the branch of mathematics and engineering in which the behavior of dynamic systems under certain input and feedback conditions is analyzed [8]. Optimal control theory, in turn, is the mathematics of calculating an optimal strategy for the input in order to achieve a minimized cost [9]. The definition of cost is problem specific, and can be minimum time, minimum fuel, minimum distance, etc.

Pontryagin’s minimum principle provides the necessary conditions for an optimal control:

Pontryagin’s minimum principle: Given an optimal solution  $\{x(\cdot), u(\cdot), t_f\}$  to Problem  $P_c$ , there exists a costate,  $\lambda(\cdot)$ , and a covector,  $\nu$ , that satisfies the Adjoint Equation, the Hamiltonian Minimization Condition, the Hamiltonian Value Condition, the Hamiltonian Evolution Equation, and the Transversality Condition [10, p.30].

The application of Pontryagin’s minimum principle to optimal control theory is discussed at length in [10], on which this introduction is based.

To illustrate the application of Pontryagin’s minimum principle, a simple example problem is considered. Consider a system whose dynamic model is a simple double integrator, as in (1.1).

$$\begin{aligned}\dot{x} &= v \\ \dot{v} &= u\end{aligned}\tag{1.1}$$



The control variable is  $u$ , which is constrained in magnitude to  $u \in [-1, 1]$ . Furthermore, let the problem be to take the system from an initial rest position to another rest position in the fastest time possible:

$$\begin{aligned}
 & \mathbf{x} = [x, v] \in \mathbb{R}^2 \\
 & \mathbf{u} = u \in [-1, 1] \\
 \text{Minimize:} \quad & J[\mathbf{x}(\cdot), \mathbf{u}(\cdot), t_f] = t_f \\
 \text{Subject to:} \quad & \dot{\mathbf{x}} = \mathbf{v} \\
 & \dot{v} = u \\
 & (x_0, v_0) = (0, 0) \\
 & (x_f, v_f) = (1, 0) \\
 & t = [0, t_f] \\
 & -1 \leq u \leq 1
 \end{aligned} \tag{1.2}$$

In (1.2),  $J$  represents the cost function, which is generally defined to be the sum of the endpoint and running costs, as seen in (1.3)

$$J[\mathbf{x}(\cdot), \mathbf{u}(\cdot), t_f] = E(\mathbf{x}(t_f), t_f) + \int_{t_0}^{t_f} F(\mathbf{x}(t), \mathbf{u}(t), t) dt \tag{1.3}$$

The first step in solving the problem is to calculate the Hamiltonian. The Hamiltonian of (1.2) is given by (1.4). In general, the Hamiltonian is also a function of time. However, this is not the case in (1.2) and thus the time variable is omitted from (1.4) for clarity.

$$\begin{aligned}
 H(\lambda, \mathbf{x}, \mathbf{u}) &= F(\mathbf{x}, \mathbf{u}) + \lambda^T f(\mathbf{x}, \mathbf{u}) \\
 H([\lambda_x, \lambda_v], [x, v], [u]) &= \lambda_x v + \lambda_v u
 \end{aligned} \tag{1.4}$$

In the Hamiltonian, the costate vector  $\lambda$  is introduced. The costate is a vector associated with the dynamics, and is related to the state variables by the adjoint equation, given by

$$-\dot{\lambda} = \frac{\partial H}{\partial \mathbf{x}} \tag{1.5}$$

The Hamiltonian minimization condition is, literally, minimization of the Hamiltonian. That is, the optimal control must minimize the Hamiltonian function over the entire time horizon. The Hamiltonian minimization condition is given by

$$\text{Min}_u \quad H([\lambda_x, \lambda_v], [x, v], [u]) = \lambda_x v + \lambda_v u$$

$$\text{Subject to:} \quad h^L \leq h(u) \leq h^U \quad (1.6)$$

Since the control signal belongs in a space bounded by inequalities,  $h(u)$  the Lagrangian of the Hamiltonian must be defined as

$$\begin{aligned} \bar{H}[\cdot] &= H[\cdot] + \mu h(u) \\ \bar{H}(\mu, \lambda, x, u) &= \lambda_x v + \lambda_v u + \mu u \end{aligned} \quad (1.7)$$

The last term includes a covector function for the control variable. The variable  $\mu$  is a time dependent Karush-Kuhn-Tucker multiplier function which is associated with the constraints on the control variable [10]. The Karush-Kuhn-Tucker condition states that (1.7) must be stationary with respect to the control. This gives the following:

$$\frac{\partial \bar{H}}{\partial u} = \lambda_v + \mu = 0 \quad (1.8)$$

For every instant in the time, the pair  $(\mu, h(u, t))$  must satisfy the complementarity condition, which is given by

$$\mu \begin{cases} \leq 0, & h(u) = h^L \\ = 0, & h^L < h(u) < h^U \\ \geq 0, & h(u) = h^U \\ \text{unrestricted}, & h^L = h^U \end{cases} \quad (1.9)$$

The complementarity condition applied to (1.8) and expressed as a condition on the velocity costate is given by

$$\lambda_v \begin{cases} \geq 0, & u(t) = -1 \\ 0, & -1 < u(t) < 1 \\ \leq 0, & u(t) = 1 \end{cases} \quad (1.10)$$



Using (1.5), the costate histories are given in (1.11), where  $a$  and  $b$  are arbitrary constants of integration.

$$\begin{aligned} -\dot{\lambda}_x &= 0 \Rightarrow \lambda_x = a \\ -\dot{\lambda}_v &= \lambda_x \Rightarrow \lambda_v = -at - b \end{aligned} \quad (1.11)$$

From (1.11), it is evident that the position and velocity costates are constant and linear, respectively, for the example problem. Assuming  $\lambda_v$  has a non-zero value over some non-zero time interval, (1.10) provides the basis for a switching function. That is, the control signal will always be positive or negative one, depending on the sign of  $\lambda_v$ . The result is summarized as

$$u(t) = \text{sgn}(at + b) \quad (1.12)$$

If there are not enough boundary conditions specified as part of problem  $P_C$ , the transversality condition may be used to solve for the additional conditions necessary to find a unique solution to the problem. The transversality condition is given by

$$\lambda(t_f) = \frac{\partial \bar{E}}{\partial x_f} \quad (1.13)$$

where

$$\bar{E}(v, x, t_f) := E(x_f, t_f) + v^T e(x_f, t_f) \quad (1.14)$$

The first term on the right side of (1.14) is the endpoint cost from (1.3). The elements of vector  $v$  are the Lagrange multipliers which are associated with the constraints  $e(x_f, t_f) = 0$ . The introduction of additional unknowns in the form of Lagrange multipliers allows any missing boundary conditions to be solved for a unique solution [10]. For the example problem given here, application of the transversality conditions yield

$$\begin{aligned}
\bar{E}(v, x, t_f) &:= t_f + v_1(x_f - x^f) + v_2(v_f - v^f) \\
\lambda_x(t_f) &= v_1 \\
\lambda_v(t_f) &= v_2
\end{aligned} \tag{1.15}$$

Since the example problem had two endpoint conditions specified for each state variable, the transversality condition does not provide any additional boundary conditions. However, since the final time is not fixed, the Hamiltonian value condition must also be examined:

$$\begin{aligned}
\bar{H}[t_f] &= -\frac{\partial \bar{E}}{\partial t_f} \\
\bar{H}[t_f] &= -1
\end{aligned} \tag{1.16}$$

From (1.16), the value of the Hamiltonian at the final time must be negative one. Finally, the Hamiltonian evolution condition must be evaluated. This is simply the time derivative of the minimized Hamiltonian, and is given as

$$\dot{\bar{H}}_{\min} = \frac{\partial \bar{H}}{\partial t} \tag{1.17}$$

The evaluation is not intuitively apparent due to the signum function. For the example problem, the solution is shown in (1.18).

$$\begin{aligned}
\dot{v} &= \text{sgn}(at + b) \\
v &= \frac{|at + b|}{a} + c \\
\lambda_x &= a \\
\lambda_v &= -at - b \\
\dot{H}^* &= \frac{\partial(\lambda_x v + \lambda_v(\text{sgn}(at + b)))}{\partial t} \\
&= \frac{\partial\left(a\left(\frac{|at + b|}{a} + c\right) + (-at - b)(\text{sgn}(at + b))\right)}{\partial t} \\
&= \frac{\partial(|at + b| + ac - |at + b|)}{\partial t} \\
&= 0
\end{aligned} \tag{1.18}$$

Despite the presence of time in the equation, the Hamiltonian does not actually explicitly depend on it. The fact that the Hamiltonian is constant at negative one is true for all minimum time problems.

While it is possible to develop and apply the necessary conditions to solve any optimal control problem, analysis quickly becomes difficult for real world problems where additional constraints and dynamic relationships must generally be introduced. Thus, numerical methods and computers are employed. One such software used to solve optimal control problems is DIDO. DIDO is a MATLAB program which solves any optimal control problem, within the bounds of proper formulation and computing power [11]. It allows complete specification of dynamics, boundary, and time variant conditions, leading to the ability to construct problems incrementally without having to come up with all new code for the problem.

THIS PAGE INTENTIONALLY LEFT BLANK

## **II. LUNAR RECONNAISSANCE ORBITER DYNAMIC MODEL**

In order to apply optimal control theory to the LRO, the S/C dynamics need to be appropriately modeled. The dynamics of a S/C are affected by properties such as geometry, motion of parts, thermal expansion, external torques, change in fuel level and distribution, etc. Modeling every parameter of such a complex system quickly makes the problem too large to solve. Thus, the important parameters to be modeled are selected and certain assumptions made to maintain the scope of the problem to a tractable size while appropriately maintaining fidelity.

The attitude control problem is defined relative to an inertial reference frame. This ensures conservation of angular momentum. The most important simplification made in this regard is that orbital velocities of the LRO around the Moon, of the Moon around the Earth, the Earth around the sun are disregarded. That is, the LRO will be modeled at a slice in time in its orbit. This allows the body frame to be treated as an inertial frame, and greatly simplifies the mathematics. Additionally, it allows for celestial objects to be modeled as being stationary in the inertial frame, simplifying the model further.

Physical properties and operational limits of the LRO were obtained via personal correspondence with the LRO program office [3], as well as open literature such as [5]. They are listed in Table 1. The inertia tensor is an estimate of the LRO at EOL. The reaction wheel capacities listed are at their operational limits, and represent a value 25 percent lower than design capacity. The power, omni antenna, and star tracker constraints are listed for completeness, but not all are implemented as constraints for maneuver design.

Table 1. LRO properties and constraints, after [3] and [5].

Inertia tensor ( $J$ )	$\begin{bmatrix} 591.47 & -20.718 & 21.459 \\ -20.718 & 849.93 & -28.031 \\ 21.459 & -28.031 & 922.51 \end{bmatrix} \text{ kg} \cdot \text{m}^2$
RW alignment ( $Z$ )	$\begin{bmatrix} 0.57357 & 0.57357 & 0.57357 & 0.57357 \\ 0.57923 & -0.57923 & -0.57923 & 0.57923 \\ 0.57923 & 0.57923 & -0.57923 & -0.57923 \end{bmatrix}$
Angular distance of S/C +z axis from sun	63 deg minimum
Maximum angular velocity of S/C ( $\omega_{\max}$ )	0.1 deg/sec per axis
Maximum angular momentum in RW ( $h_{\max}$ )	60 N-m-s each
Maximum RW control torque ( $\tau_{\max}$ )	0.16 N-m each
Power constraint	-y axis preferred toward sun
Omni antenna constraint	Earth placed in preferred quadrant of S/C x-y plane
Star tracker constraint	Field of view of star trackers 25 deg from sun, 15 deg from Moon, and 15 deg from Earth

The key tenet of this thesis lies in the pointing constraints. The aim is to perform simulations that involve avoidance maneuvers, so that an approach can be developed for their automation. Therefore, a maneuver scenario must be developed which would violate a pointing constraint if no action is taken. To do this, first, one of the pointing constraints is defined in the problem. As per Table 1, the sensitive instruments located on the +z face of the S/C must stand off from

the sun by 63 degrees. Therefore, the problem is defined such that the S/C +z axis must remain 63 degrees or more away from the direction of the sun.

The spacecraft dynamics must also be defined. Quaternions are chosen to represent the S/C attitude. Since the LRO uses RWs as its only means of attitude control, the combination of (2.1) and (2.2) is used as the dynamic model [12]. The controls are defined to be the RW torques, as seen in (2.3). This assumes a rigid body S/C and that relative motion of the RWs is negligible.

$$\begin{aligned}\dot{q}_1 &= \frac{1}{2}(\omega_1 q_4 - \omega_2 q_3 + \omega_3 q_2) \\ \dot{q}_2 &= \frac{1}{2}(\omega_1 q_3 + \omega_2 q_4 - \omega_3 q_1) \\ \dot{q}_3 &= \frac{1}{2}(-\omega_1 q_2 + \omega_2 q_1 + \omega_3 q_4) \\ \dot{q}_4 &= \frac{1}{2}(-\omega_1 q_1 - \omega_2 q_2 + \omega_3 q_3)\end{aligned}\tag{2.1}$$

$$\dot{\omega} = -J^{-1}(\omega \times (J\omega + Zh) + Zh\dot{h})\tag{2.2}$$

$$\dot{h} = u\tag{2.3}$$

Next, the boundary conditions are defined. The required specifications consist of an initial and end attitude in quaternions, initial and end S/C angular rates, and an initial RW momentum vector. It is not necessary to define a final RW momentum vector, as it is implicitly specified via conservation of angular momentum in the inertial frame. The initial attitude is defined to allow the body frame to coincide with the inertial frame. This allows the reconstruction of the actual maneuvers used on the LRO to be done more easily, as discussed in Chapter III.

Lastly, a procedure for implementing the pointing constraint needs to be defined. To do this, a path constraint can be introduced, which relies on the direction of the sun in the inertial frame. Since the direction of the sensitive instruments is defined in the body frame, the instrument vector must be converted to a vector in the inertial frame by using a DCM derived from

quaternions as in (2.4), where  $\hat{e}^B$  is a unit vector expressed in the body frame,  $\hat{e}^N$  is the same vector expressed in the inertial frame, and the quaternions describe the relative orientation of the body frame with respect to the inertial frame [12]. This is a coordinate transformation, wherein a coordinate system is rotated about an axis of rotation and angle described by a quaternion. Since the S/C +z vector is  $[0 \ 0 \ 1]^T$  in the body frame, the S/C +z vector expressed in the inertial frame is given by the last column of (2.4).

$$\hat{e}^N = \begin{bmatrix} q_1^2 - q_2^2 - q_3^2 + q_4^2 & 2(q_1q_2 + q_3q_4) & 2(q_1q_3 - q_2q_4) \\ 2(q_1q_2 - q_3q_4) & -q_1^2 + q_2^2 - q_3^2 + q_4^2 & 2(q_2q_3 + q_1q_4) \\ 2(q_1q_3 + q_2q_4) & 2(q_2q_3 - q_1q_4) & -q_1^2 - q_2^2 + q_3^2 + q_4^2 \end{bmatrix} \hat{e}^B \quad (2.4)$$

By utilizing the definition of the dot product, the angle between two unit vectors  $\hat{S}$  and  $\hat{z}$  can be calculated as (2.5). A graphical representation of this relationship is shown in Figure 2.

$$\theta = \cos^{-1}(\hat{S} \cdot \hat{z}) \quad (2.5)$$

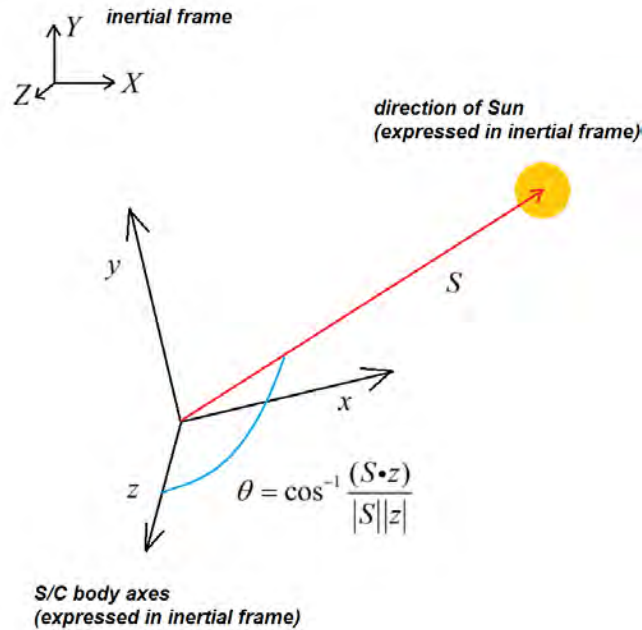


Figure 2. Illustration of sun avoidance angle calculation.



### **III. RECONSTRUCTION OF EXISTING SLEW ALGORITHM**

To establish a baseline with which optimal control results shall be compared, the actual types of maneuvers used on the LRO must be recreated. In general, the LRO utilizes the eigenaxis slew to perform point to point slews [5]. An eigenaxis maneuver is one in which the axis of rotation is held constant. The advantage of an eigenaxis maneuver is the fact that the angle of rotation between any two attitudes is minimized, but this does not necessarily translate to a minimum fuel or minimum time maneuver [13]-[15]. Hereafter, an eigenaxis slew that takes the S/C from a one defined orientation to another will be referred to as a direct slew [5].

The maneuver of the LRO increases in complexity when a pointing constraint is introduced. For example, if a direct slew causes sensitive instruments to point at the sun at any instant, then the maneuver cannot be performed. A trial and error approach is used to determine the appropriate maneuver, as described in [5] and explained below.

Consistent with [5], the term minimum slew will be used to designate a maneuver such that a specific vector in the S/C body frame, such as the vector representing the direction that instruments may be pointing, is slewed point to point. This is also an eigenaxis maneuver, but it differs from a direct slew in that only one vector of the S/C is examined as opposed to the entire coordinate frame. A minimum slew allows, for example, changing the direction that instruments are pointing without regard to the specific orientation of the entire S/C.

In all approaches for avoiding violation of a pointing constraint, the slew is broken up into two segments. Let the direction that an axis of concern is pointing at the beginning of a maneuver be called “Point A” and at the end, “Point B.” The path between Point A and Point B represents the direction that the axis of

interest points during the maneuver. In an eigenaxis maneuver, this path will be a portion of a great circle. Let the midpoint of this arc be denoted as “Point C.”

The first attempt to break up the maneuver utilizes a minimum slew of the axis of interest from Point A to Point C, and then a direct slew to take the S/C to its desired final orientation. If this maneuver still causes a pointing constraint violation, then the order is swapped. That is, the direct slew is performed first.

If the first method of mitigation fails, the next step is to move Point C away from the center of the obstacle by 30 degrees. The combinations of minimum and direct slews are then investigated. If the constraint is still violated, Point C is now moved 60 degrees away from the center of the obstacle, and the process repeated. The two stage maneuvers will hereafter collectively be called “dogleg” maneuvers.

To illustrate the application of this idea, the initial and final attitudes as well as the direction of the sun are chosen such that a direct slew will cause the +z axis of the spacecraft to point toward the sun. This will violate the standoff constraint for sensitive instruments (See Table 1). The specific attitude values for this example maneuver are detailed in Table 2. When the aforementioned protocol is followed to mitigate this violation, the first mitigation method to yield a satisfactory solution is to move Point C by 30 degrees from its original location, and then to perform a minimum slew followed by a direct slew. The original and modified maneuvers are shown in Figure 3.

Table 2. Boundary conditions for example sun avoidance maneuver.

$q_0$	$[0, 0, 0, 1]^T$
$q_f$	$[0.400, -0.800, 0.4279, 0.130]^T$
$\omega_0 = \omega_f$	$[0, 0, 0]^T$ deg/ sec

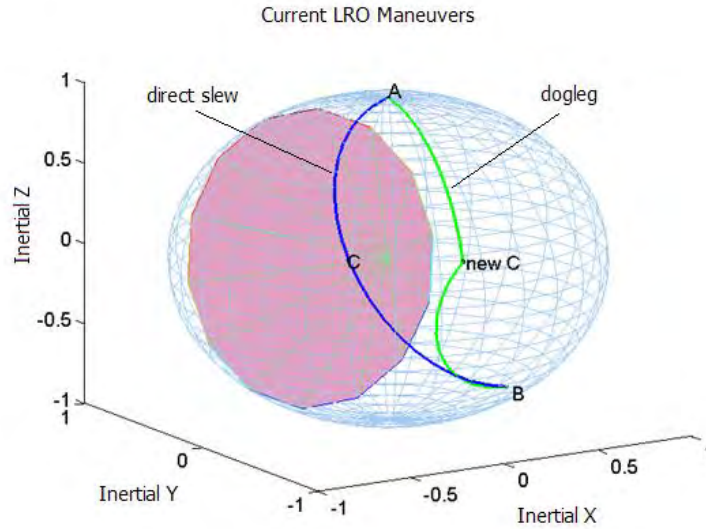


Figure 3. Direct slew and dogleg maneuver.

Figure 3 shows the motion of the +z axis of the spacecraft, as well as a cone depicting a 63 degree half angle from the direction of the sun. Thus, if the path of the +z axis goes inside the projection of the red cone, representing the standoff range, there is a constraint violation. The dogleg maneuver is clearly able to avoid the pointing violation that occurs with a simple direct slew. The numerical values of the angle between the S/C +z axis and the sun are shown in Figure 4.

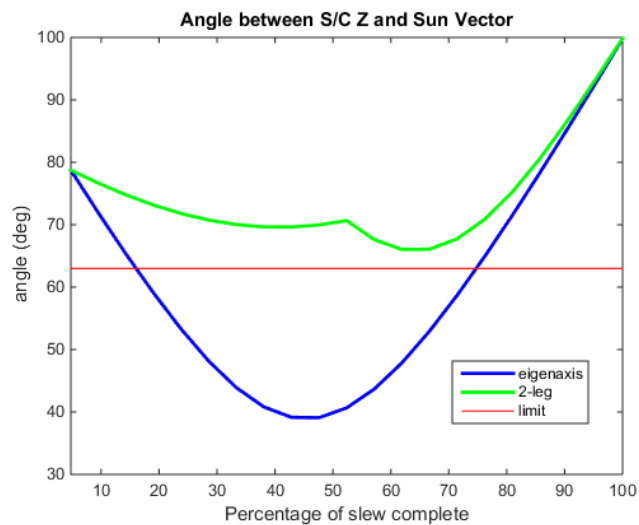


Figure 4. Angular proximity of +z axis to center of sun avoidance cone.

## A. BASELINE MANEUVER PERFORMANCE

In order to quantify the performance difference between the existing and optimal control maneuvers, the time it takes to complete the existing maneuver will be estimated. To simplify the calculation, angular acceleration is assumed to be infinite. This allows for the calculation to be reduced to an angular distance and velocity.

In a quaternion, the first three elements encode a unit vector  $\hat{e}$ , which is the axis of rotation, while the last element represents the angle of rotation of a frame about this axis, as shown in (3.1). The axis of rotation is broken down into components expressed in the inertial frame.

$$q = \begin{bmatrix} \hat{e}_1 \sin(\frac{\theta}{2}) \\ \hat{e}_2 \sin(\frac{\theta}{2}) \\ \hat{e}_3 \sin(\frac{\theta}{2}) \\ \cos(\frac{\theta}{2}) \end{bmatrix} \quad (3.1)$$

Let  $q'$  and  $q''$  represent consecutive, separate coordinate rotations. Then the equivalent quaternion  $q$  can be found using equation (3.2) [12]. The equation has been arranged such that the quaternion for the second coordinate transformation is isolated for path recreation.

$$q'' = \begin{bmatrix} q'_4 & q'_3 & -q'_2 & q'_1 \\ -q'_3 & q'_4 & q'_1 & q'_2 \\ q'_2 & -q'_1 & q'_4 & q'_3 \\ -q'_1 & -q'_2 & -q'_3 & q'_4 \end{bmatrix}^{-1} \begin{bmatrix} q_1 \\ q_2 \\ q_3 \\ q_4 \end{bmatrix} \quad (3.2)$$

Since the initial conditions of the problem dictate that the S/C body frame be coincident with the Inertial frame, the relationship given in (3.1) allows a simple calculation of the angle of rotation for the direct slew. Furthermore, the angular velocity of the S/C about each axis must be proportional to the

components of the axis of rotation expressed in the body frame, as in (3.3). An easy way to visualize this is to simply assume a rotation about the inertial +X axis. Since the body frame and inertial frame are originally coincident, it follows that the S/C must rotate about its +x axis for this maneuver. By setting the axis with the largest sectorial component to 0.1 degrees/sec, the maximum angular velocity for the slew can be calculated.

$$\begin{bmatrix} \omega_x \\ \omega_y \\ \omega_z \end{bmatrix} = k \begin{bmatrix} \hat{e}_1 \\ \hat{e}_2 \\ \hat{e}_3 \end{bmatrix} \quad (3.3)$$

where

$$k = \frac{0.1 \text{ deg/s}}{\max\{|\hat{e}_1|, |\hat{e}_2|, |\hat{e}_3|\}}$$

For the dogleg maneuver, it is necessary to find the new location of Point C. First, the original Point C is found by finding the direction of the S/C +z axis at the midpoint of the direct slew. This is done by using (3.1), using half of the original angle for the fourth component and normalizing to ensure that  $\sum_{i=1}^4 q_i^2 = 1$ . This quaternion is then substituted into (2.4) to locate the S/C +z axis at the midpoint of rotation, which by definition is Point C.

To rotate this point 30 degrees away from the center of the obstacle, the vector corresponding to Point C is rotated about an axis perpendicular to the center of the obstacle and Point C. Let  $\hat{C}$  represent the original direction of Point C in the inertial frame,  $\hat{S}$  the direction of the sun, and  $\hat{e}_c$  the axis about which Point C will be rotated. Then, the axis of this rotation can be found by using (3.4). By again applying the coordinate transformation of equation (2.4) using 30 degrees as the angle of rotation, the unit vector pointing at the new Point C, heretofore referred to as  $\hat{\hat{C}}$  is located. Figure 5 shows an illustration of this process.

$$\hat{e}_c = \frac{\hat{S} \times \hat{C}}{|\hat{S} \times \hat{C}|} \quad (3.4)$$

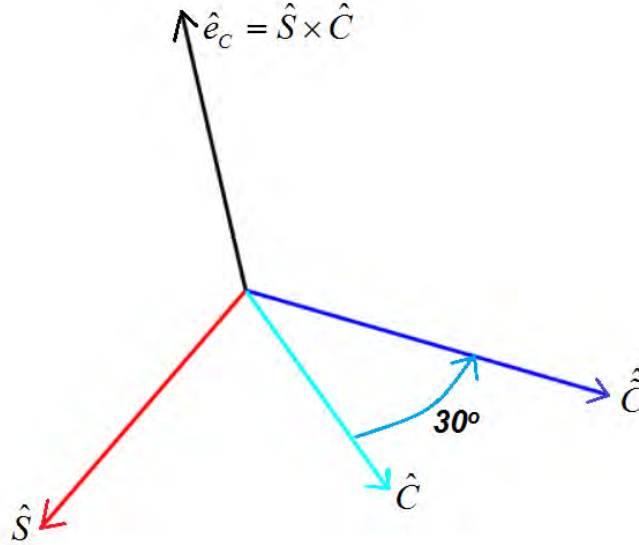


Figure 5. Process of locating  $\hat{C}$ .

Since the first leg is a minimum slew, the axis of rotation of the S/C body frame is found by taking the cross product of the vectors corresponding to the initial and final directions of the S/C Z-axis, expressed in the inertial frame. For the second leg, the relationship in (3.2) is used to calculate the quaternion representing only the second leg of the maneuver. The axis of rotation for the second maneuver is expressed in the S/C body frame using equation (2.4), after which equation (3.3) is used to determine the S/C angular velocities.

The angular lengths and maneuver times of the baseline direct slew and dogleg maneuvers are detailed in Table 3. For further analysis and comparison, the total time for the dogleg maneuver is used, which is 1,975 seconds. Note that the dogleg maneuver takes 48 percent longer than the direct slew, which could

mean that an opportunity for science collection could be lost. This motivates the desire to perform a sun avoidance slew in the least amount of time.

Table 3. Estimates of status quo maneuver times.

<b>Maneuver</b>	<b>Angular Length (deg)</b>	<b>Time (sec)</b>
<i>Direct slew</i>	165	1,331
Dogleg leg 1 (minimum)	74	764
Dogleg leg 2 (direct)	128	1,211
<i>Dogleg (total)</i>	202	1,975

THIS PAGE INTENTIONALLY LEFT BLANK



## IV. AUTOMATED MANEUVER DESIGN AND CHECKOUT

The dynamic model constructed in Chapter III as well as the constraints introduced are now used to develop an optimal control problem for automated maneuver design. This chapter introduces the optimal control model and adjustments that were made to ensure proper formulation was present to obtain flight ready solutions. Automation is used in the sense that an avoidance maneuver can be designed without resorting to the heuristic steps described in Chapter III. Since the maneuver design is obtained as the solution to an optimal control problem, human intervention is not required to generate the slew. Moreover, the maneuver will also automatically satisfy the vehicle's dynamic constraints, a feature that can be leveraged to help facilitate the pre-flight maneuver checkout.

### A. OPTIMAL CONTROL PROBLEM

From the conditions described in Chapter II, the optimal control problem statement becomes:

$$\begin{aligned}x &= [q, \omega, h] \in \mathfrak{R}^{11} \\ u &\in \mathfrak{R}^4\end{aligned}$$

Minimize:

$$J[x(\cdot), u(\cdot), t_f] = t_f$$

Subject to:

$$\begin{aligned}
q_1 &= \frac{1}{2}(\omega_1 q_4 - \omega_2 q_3 + \omega_3 q_2) \\
q_2 &= \frac{1}{2}(\omega_1 q_3 + \omega_2 q_4 - \omega_3 q_1) \\
q_3 &= \frac{1}{2}(-\omega_1 q_2 + \omega_2 q_1 + \omega_3 q_4) \\
q_4 &= \frac{1}{2}(-\omega_1 q_1 - \omega_2 q_2 + \omega_3 q_3) \\
\omega &= -J^{-1}(\omega \times (J\omega + Zh) + Zh) \\
h &= u \\
t &= [0, t_f] \\
(q_0, \omega_0, h_0) &= [q_0, \omega_0, h_0] \\
(q_f, \omega_f) &= [q_f, \omega_f] \\
|h_i| &\leq 60 N \cdot m \cdot s \\
|\dot{h}_i| &\leq 0.16 N \cdot m \\
|\omega_i| &\leq 0.1 \text{ deg/s} \\
|\theta| &\geq 63 \text{ deg}
\end{aligned} \tag{4.1}$$

where the sun avoidance angle is given as:

$$\theta = \cos^{-1}(\hat{S} \cdot \hat{z})$$

In (4.1), the two vector quantities represent the direction of the sun ( $\hat{S}$ ) and the direction of the S/C +z axis ( $\hat{z}$ ), both expressed in the inertial frame.

## 1. Necessary Conditions

The Hamiltonian for problem (4.1) is given by (4.2). The variable  $\lambda$  refers to the costate variable, with the corresponding state variable listed as a subscript. Due to the cross product terms present in the dynamic equations, there are myriad terms in the Hamiltonian, and it is almost impossible to determine by inspection the effects that the different variables may have on the Hamiltonian.

$$\begin{aligned}
H = & \lambda_{h_1} u_1 + \lambda_{h_2} u_2 + \lambda_{h_3} u_3 + \lambda_{h_4} u_4 \\
& + \frac{1}{\#1} \left[ -\lambda_{\omega_3} \left( (J_{xx} J_{yy} - J_{xy} J_{yx})(\#4) - (J_{xx} J_{zy} - J_{xy} J_{zx})(\#3) + (J_{yx} J_{zy} - J_{yy} J_{zx})(\#2) \right) \right. \\
& + \lambda_{\omega_2} \left( (J_{xx} J_{yz} - J_{xz} J_{yx})(\#4) - (J_{xx} J_{zz} - J_{xz} J_{zx})(\#3) + (J_{yx} J_{zz} - J_{yz} J_{zx})(\#2) \right) \\
& \left. - \lambda_{\omega_1} \left( (J_{xy} J_{yz} - J_{xz} J_{yy})(\#4) - (J_{xy} J_{zz} - J_{xz} J_{zy})(\#3) + (J_{yy} J_{zz} - J_{yz} J_{zy})(\#2) \right) \right] \\
& + \frac{1}{2} \left[ \lambda_{q_1} (q_2 \omega_3 - q_3 \omega_2 + q_4 \omega_1) + \lambda_{q_2} (q_3 \omega_1 - q_1 \omega_3 + q_4 \omega_2) \right. \\
& \left. + \lambda_{q_3} (q_1 \omega_2 - q_2 \omega_1 + q_4 \omega_3) - \lambda_{q_4} (q_1 \omega_1 + q_2 \omega_2 + q_3 \omega_3) \right]
\end{aligned} \tag{4.2}$$

where

$$\begin{aligned}
\#1 &= J_{xx} J_{yy} J_{zz} - J_{xx} J_{yz} J_{zy} - J_{xy} J_{yx} J_{zz} + J_{xy} J_{yz} J_{zx} + J_{xz} J_{yx} J_{zy} - J_{xz} J_{yy} J_{zx} \\
\#2 &= \omega_2 (\#5) - \omega_3 (\#6) + Z_{11} u_1 + Z_{12} u_2 + Z_{13} u_3 + Z_{14} u_4 \\
\#3 &= \omega_3 (\#7) - \omega_1 (\#5) + Z_{21} u_1 + Z_{22} u_2 + Z_{23} u_3 + Z_{24} u_4 \\
\#4 &= \omega_1 (\#6) - \omega_2 (\#7) + Z_{31} u_1 + Z_{32} u_2 + Z_{33} u_3 + Z_{34} u_4 \\
\#5 &= J_{zx} \omega_1 + J_{zy} \omega_2 + J_{zz} \omega_3 + Z_{31} h_1 + Z_{32} h_2 + Z_{33} h_3 + Z_{34} h_4 \\
\#6 &= J_{yx} \omega_1 + J_{yy} \omega_2 + J_{yz} \omega_3 + Z_{21} h_1 + Z_{22} h_2 + Z_{23} h_3 + Z_{24} h_4 \\
\#7 &= J_{xx} \omega_1 + J_{xy} \omega_2 + J_{xz} \omega_3 + Z_{11} h_1 + Z_{12} h_2 + Z_{13} h_3 + Z_{14} h_4
\end{aligned}$$

Hamiltonian minimization yields switching functions for all four controls, since these appear linearly. When the first switching function is positive, the  $u_1$  is the maximum negative value, and vice versa. Similar results follow for the other controls. The adjoint equations are:

$$\begin{aligned}
\lambda_{q_1} &= \frac{1}{2}(\lambda_{q_3} \omega_1 - \lambda_{q_1} \omega_3 + \lambda_{q_4} \omega_2) \\
\lambda_{q_2} &= \frac{1}{2}(\lambda_{q_1} \omega_2 - \lambda_{q_1} \omega_3 + \lambda_{q_4} \omega_3) \\
\lambda_{q_3} &= \frac{1}{2}(-\lambda_{q_1} \omega_1 - \lambda_{q_2} \omega_2 - \lambda_{q_3} \omega_3) \\
\lambda_{q_4} &= \frac{1}{2}(\lambda_{q_2} \omega_3 - \lambda_{q_3} \omega_2 + \lambda_{q_4} \omega_1) \\
\lambda_{\omega_1} &= \frac{1}{2}(\lambda_{q_3} q_2 - \lambda_{q_2} q_3 - \lambda_{q_1} q_4 + \lambda_{q_4} q_1) + \frac{1}{\#1} [\lambda_{\omega_3} (\#16\#5 + \#13\#3 - \#10\#17) \\
&\quad - \lambda_{\omega_2} (\#15\#5 + \#12\#3 - \#9\#17) + \lambda_{\omega_1} (\#14\#5 + \#11\#3 - \#8\#17)] \\
\lambda_{\omega_2} &= \frac{1}{2}(\lambda_{q_1} q_3 - \lambda_{q_3} q_1 - \lambda_{q_2} q_4 + \lambda_{q_4} q_2) + \frac{1}{\#1} [\lambda_{\omega_3} (\#16\#7 + \#10\#2 - \#13\#18) \\
&\quad + \lambda_{\omega_2} (\#15\#7 + \#9\#2 - \#12\#18) + \lambda_{\omega_1} (\#14\#7 + \#8\#2 - \#11\#18)] \\
\lambda_{\omega_3} &= \frac{1}{2}(\lambda_{q_2} q_1 - \lambda_{q_1} q_2 - \lambda_{q_3} q_4 - \lambda_{q_4} q_3) + \frac{1}{\#1} [\lambda_{\omega_3} (\#13\#6 + \#10\#4 - \#16\#19) \\
&\quad - \lambda_{\omega_2} (\#12\#6 + \#9\#4 - \#15\#19) + \lambda_{\omega_1} (\#11\#6 + \#8\#4 - \#14\#19)] \\
\lambda_{h_1} &= \frac{1}{\#1} [\lambda_{\omega_2} (\#15\#31 + \#12\#27 + \#9\#23) - \lambda_{\omega_3} (\#16\#31 + \#13\#27 + \#10\#23) \\
&\quad - \lambda_{\omega_1} (\#14\#31 + \#11\#27 + \#8\#23)] \\
\lambda_{h_2} &= \frac{1}{\#1} [\lambda_{\omega_2} (\#15\#30 + \#12\#26 + \#9\#22) - \lambda_{\omega_3} (\#16\#30 + \#13\#26 + \#10\#22) \\
&\quad - \lambda_{\omega_1} (\#14\#30 + \#11\#26 + \#8\#22)] \\
\lambda_{h_3} &= \frac{1}{\#1} [\lambda_{\omega_2} (\#15\#29 + \#12\#25 + \#9\#21) - \lambda_{\omega_3} (\#16\#29 + \#13\#25 + \#10\#21) \\
&\quad - \lambda_{\omega_1} (\#14\#29 + \#11\#25 + \#8\#21)] \\
\lambda_{h_4} &= \frac{1}{\#1} [\lambda_{\omega_2} (\#15\#28 + \#12\#24 + \#9\#20) - \lambda_{\omega_3} (\#16\#28 + \#13\#24 + \#10\#20) \\
&\quad - \lambda_{\omega_1} (\#14\#28 + \#11\#24 + \#8\#20)]
\end{aligned} \tag{4.3}$$

where

$$\begin{aligned}
\#1 &= J_{xx}J_{yy}J_{zz} - J_{xx}J_{yz}J_{zy} - J_{xy}J_{yx}J_{zz} + J_{xy}J_{yz}J_{zx} + J_{xz}J_{yx}J_{zy} - J_{xz}J_{yy}J_{zx} \\
\#2 &= J_{zx}\omega_1 - J_{yy}\omega_3 + 2J_{zy}\omega_2 + J_{zz}\omega_3 + Z_{31}h_1 + Z_{32}h_2 + Z_{33}h_3 + Z_{34}h_4 \\
\#3 &= 2J_{zx}\omega_1 - J_{xx}\omega_3 + J_{xx}\omega_2 + J_{zz}\omega_3 + Z_{31}h_1 + Z_{32}h_2 + Z_{33}h_3 + Z_{34}h_4 \\
\#4 &= J_{yx}\omega_1 + J_{yy}\omega_2 + 2J_{zy}\omega_3 - J_{zz}\omega_2 + Z_{21}h_1 + Z_{22}h_2 + Z_{23}h_3 + Z_{24}h_4 \\
\#5 &= 2J_{yx}\omega_1 - J_{xx}\omega_2 + J_{yy}\omega_2 + J_{yz}\omega_3 + Z_{21}h_1 + Z_{22}h_2 + Z_{23}h_3 + Z_{24}h_4 \\
\#6 &= J_{xx}\omega_1 + J_{xy}\omega_2 + 2J_{xz}\omega_3 - J_{zz}\omega_1 + Z_{11}h_1 + Z_{12}h_2 + Z_{13}h_3 + Z_{14}h_4 \\
\#7 &= J_{xx}\omega_1 + 2J_{xy}\omega_2 + J_{xz}\omega_3 - J_{yy}\omega_1 + Z_{11}h_1 + Z_{12}h_2 + Z_{13}h_3 + Z_{14}h_4 \\
\#8 &= J_{yy}J_{zz} - J_{yz}J_{zy} \\
\#9 &= J_{yx}J_{zz} - J_{yz}J_{zx} \\
\#10 &= J_{yx}J_{zy} - J_{yy}J_{zx} \\
\#11 &= J_{xy}J_{zz} - J_{xz}J_{zy} \\
\#12 &= J_{xx}J_{zz} - J_{xz}J_{zx} \\
\#13 &= J_{xx}J_{zy} - J_{xy}J_{zx} \\
\#14 &= J_{xy}J_{yz} - J_{xz}J_{yy} \\
\#15 &= J_{xx}J_{yz} - J_{xz}J_{yx} \\
\#16 &= J_{xx}J_{yy} - J_{xy}J_{yx} \\
\#17 &= J_{yx}\omega_3 - J_{zx}\omega_2 \\
\#18 &= J_{xy}\omega_3 - J_{zy}\omega_1 \\
\#19 &= J_{xz}\omega_2 - J_{yz}\omega_1 \\
\#20 &= Z_{24}\omega_3 - Z_{34}\omega_2 \\
\#21 &= Z_{23}\omega_3 - Z_{33}\omega_2 \\
\#22 &= Z_{22}\omega_3 - Z_{32}\omega_2 \\
\#23 &= Z_{21}\omega_3 - Z_{31}\omega_2 \\
\#24 &= Z_{14}\omega_3 - Z_{34}\omega_1 \\
\#25 &= Z_{13}\omega_3 - Z_{33}\omega_1 \\
\#26 &= Z_{12}\omega_3 - Z_{32}\omega_1 \\
\#27 &= Z_{11}\omega_3 - Z_{31}\omega_1 \\
\#28 &= Z_{14}\omega_2 - Z_{24}\omega_1 \\
\#29 &= Z_{13}\omega_2 - Z_{23}\omega_1 \\
\#30 &= Z_{12}\omega_2 - Z_{22}\omega_1 \\
\#31 &= Z_{11}\omega_2 - Z_{21}\omega_1
\end{aligned}$$

The adjoint equations of (4.4) can be used to verify the proper trajectories for the costates. Evaluation of the transversality condition yields some information that will augment the information in (4.4) and is useful for checking optimality. Specifically,  $\lambda_{h_1}(t_f) = \lambda_{h_2}(t_f) = \lambda_{h_3}(t_f) = \lambda_{h_4}(t_f) = 0$ . The final condition useful for checking optimality comes from the Hamiltonian value condition, which as shown in (1.16) is a constant negative one for a minimum time problem.

## **B. MANEUVER CHECKOUT METHODOLOGY**

In keeping with good engineering practice, several methods of V&V are used for the checkout for the optimal control solutions. The first of these is to verify that the magnitude of the quaternion vector is always unity. This condition is expressly imposed in the coding of the problem for solving in DIDO. Any deviation of the magnitude from one beyond that expected from machine rounding would be an immediate red flag that the solution is invalid.

The second method of V&V is an inspection of the Hamiltonian. Since (4.1) is a minimum time problem, the Hamiltonian value condition and Hamiltonian evolution condition specify that the Hamiltonian should be a constant at negative one. This is a very simple and powerful check.

The third V&V method is to verify the conditions obtained via the transversality equations. The transversality equations specified that the momentum costates are equal to zero at the conclusion of the maneuver. This is another necessary condition that is easy to check.

The final and most involved V&V check is a propagation of the solution controls using a simple Simulink model of the LRO. The Simulink model will use interpolated control signals as control input. The LRO dynamics will be simulated, and rates integrated over time to produce propagated solutions to attitude, angular velocity, and RW momentum. A pictorial view of the Simulink model is shown in Figure 6. Quaternions, S/C angular velocities, and RW momenta with respect to time will be plotted and checked against the expected results.

In addition to verifying that the occultation constraints are satisfied for each solution, the checkout exercises described above can be used to automate the maneuver checkout process. Suitable tolerances for each V&V step can be imposed by the S/C operators. If these tolerances are met, then the maneuver can be considered as flight ready as far as LRO dynamic feasibility is concerned.

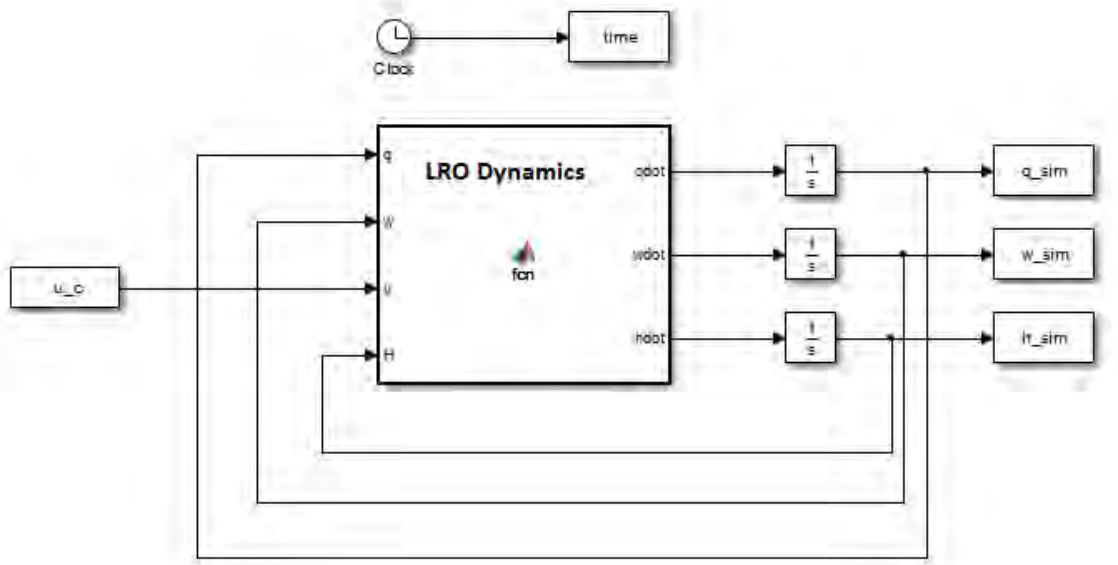


Figure 6. Simulink propagator used for maneuver checkout.

### C. INITIAL RESULTS

The initial optimal control problem was solved using DIDO software. The resulting trajectories of the primary axes of the S/C are shown in Figure 7. The angular distance of the S/C +z axis from the sun is shown in Figure 8. The angular velocity of the S/C, momentum in each RW, and the solved control signals are shown in Figures 9, 10, and 11, respectively. The total maneuver time is 1,135 seconds, which represents a 43 percent improvement over the status quo approach (see Table 3).

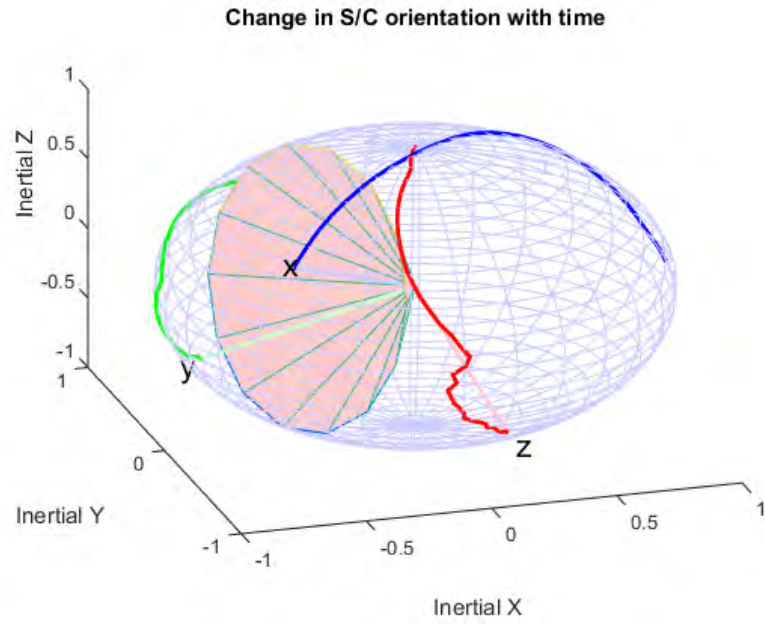


Figure 7. S/C orientation evolution for initial problem formulation.

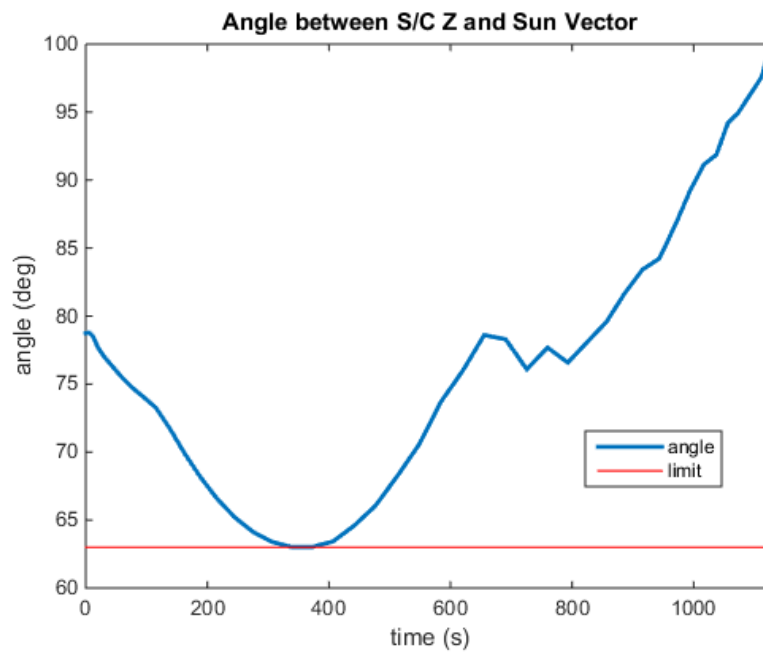


Figure 8. Angle between S/C +z axis and sun vector for initial problem formulation.



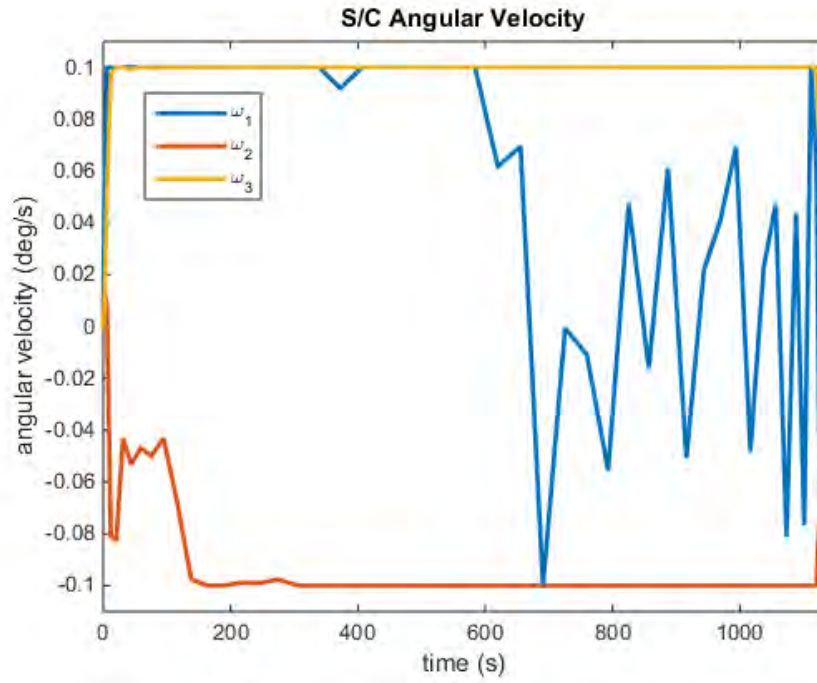


Figure 9. S/C angular velocity evolution for initial problem formulation.

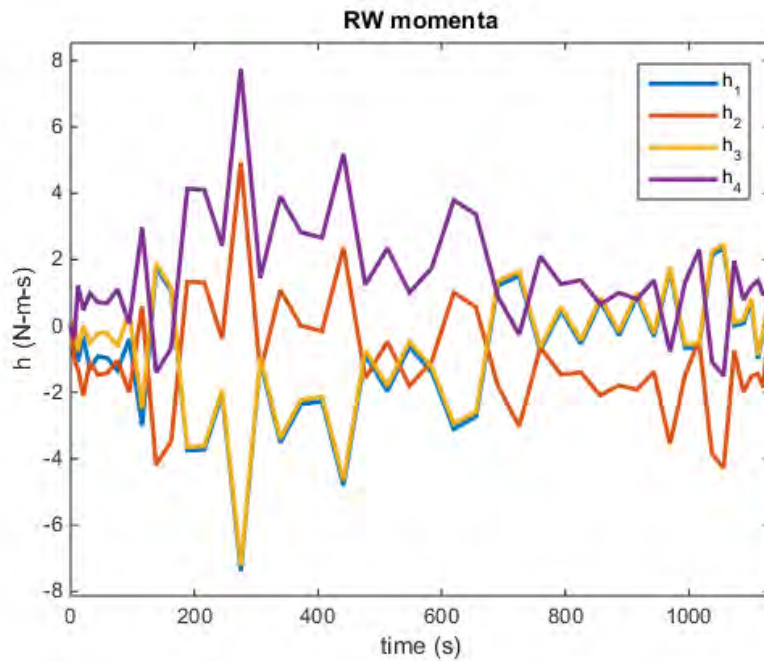


Figure 10. RW momentum storage for initial problem formulation.

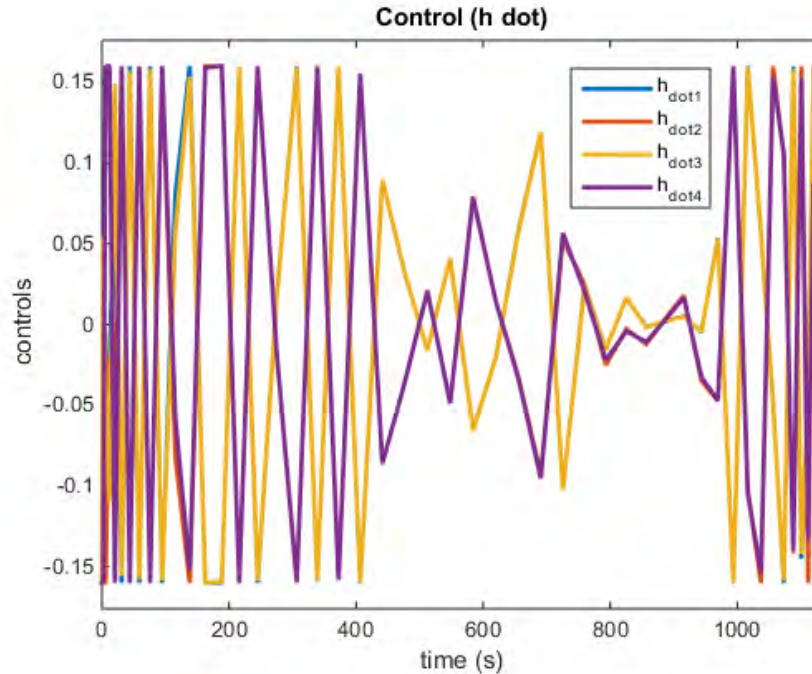


Figure 11. Control signals for initial problem formulation.

As seen in Figures 7 and 8, the optimal control problem allows the S/C +z axis to come up to the limits of a pointing violation, without violating the constraint. Comparing with the direct slew and dogleg maneuvers shown in Figure 3, the improvement appears obvious. While the solution is an optimal solution within the limits of computational fidelity, it is far from a good solution from the perspective of implementation. The control signal (see Figure 11) rapidly oscillates between the maximum positive and negative values, which is a possible indication that active control is not needed during those times and can be zeroed out. This in turn would have the effect of smoothing the RW momentum and S/C rate trajectories.

The results are a good illustration on how an improperly specified problem can lead to subpar results. Pseudospectral methods are a very strong tool to use in solving control problems, but the tools are useless if not used properly.

A readily apparent problem is that most of the changes in the controls occur during a small fraction of time at the beginning and end of the simulation.

This is due to the relatively large angle through which the S/C must slew compared to the small angular velocity limit. When DIDO performs its algorithms, it breaks up the time space into a number of smaller nodes defined by the user. With increasing node count, the time spent on calculations increases exponentially and quickly becomes impractical. For this simulation, the node count was 50, and the time it took to solve on the computer was over nine hours. Not only is this an impractically long time, but the node count used is actually insufficient for a proper solution.

The solution is point-wise and must be interpolated between nodes. That is, the solution is actually discrete and not continuous. When only a small fraction of the time space is devoted to meaningful control, these discrete time pieces lack the resolution to capture appropriate changes needed for a good solution.

Another issue with the abovementioned solution is the non-smooth nature of the RW momenta curves. This points to the controls being possibly unnecessarily actuated in opposite directions. Due to the bound on control signals, the problem formulation yields switching functions. If the switching function over time is oscillating about zero, the switch can for all practical purposes be set to zero. That is, the control signal can be set to zero. A section of the plot of the switching function associated with the first control signal is shown in Figure 12. In this portion, the switching function is seen to take on very small positive and negative values. If these are presumed to be zero, simplifying the control signal into a bang-off-bang type profile, ostensibly the results will be better behaved. This behavior can also be corrected with a better problem scaling.

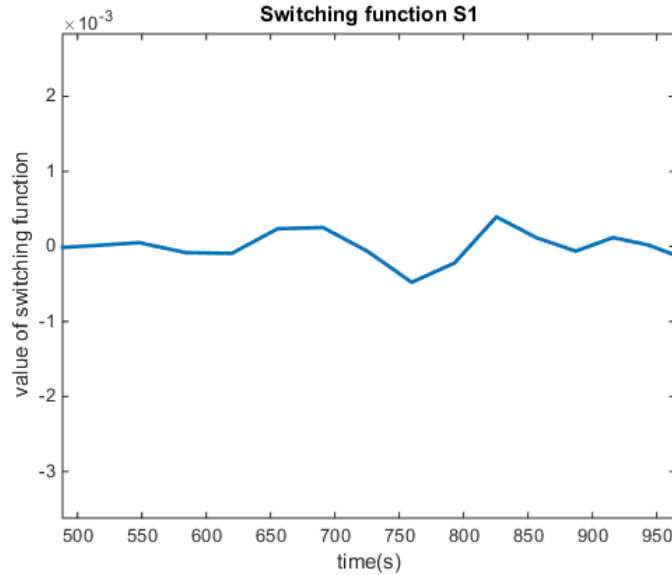


Figure 12. Switching function for first control for initial problem formulation.

#### D. MODIFICATIONS TO OPTIMAL CONTROL PROBLEM

The combination of the size of the discrete time steps and the angular velocity limit of the S/C causes the solution to look undesirable, as discussed above. The S/C accelerates in rotation to its limit in a very short time relative to the solution time space and then coasts most of the way until it decelerates in a very short relative time. Thus, some modifications to the problem specifications are considered to allow a more effective approach to the optimal control problem. Specifically, the issues of problem scaling and the specification of angular velocity limits are examined. The switching function will be maintained, as the removal of the angular velocity specification will help remedy this issue.

##### 1. Scaling

The main problem with the existing problem formulation is that it is poorly scaled. As seen in (4.2), many product terms exist between various state and costate variables. This means that if the magnitudes of these variables vary greatly, the problem can potentially become very sensitive to slight perturbations, leading to a poor solution.

A method to mitigate the issue of poor scaling is to compare the state variables to their corresponding costate variables. By roughly matching the orders of magnitudes between the pairs of variables, the problem becomes better scaled. An additional benefit of better scaling is that the calculation time for obtaining a solution is significantly reduced. Plots of the rate costates and the Hamiltonian for the problem prior to scaling are shown in Figures 13 and 14. The Hamiltonian for a minimum time problem should be negative one. However, as seen in Figure 14, the actual Hamiltonian takes on values that deviate from negative one by orders of magnitude including a peak to almost 14,000. The costates compared with their corresponding states in Figure 9 make apparent the disparity in order of magnitude.

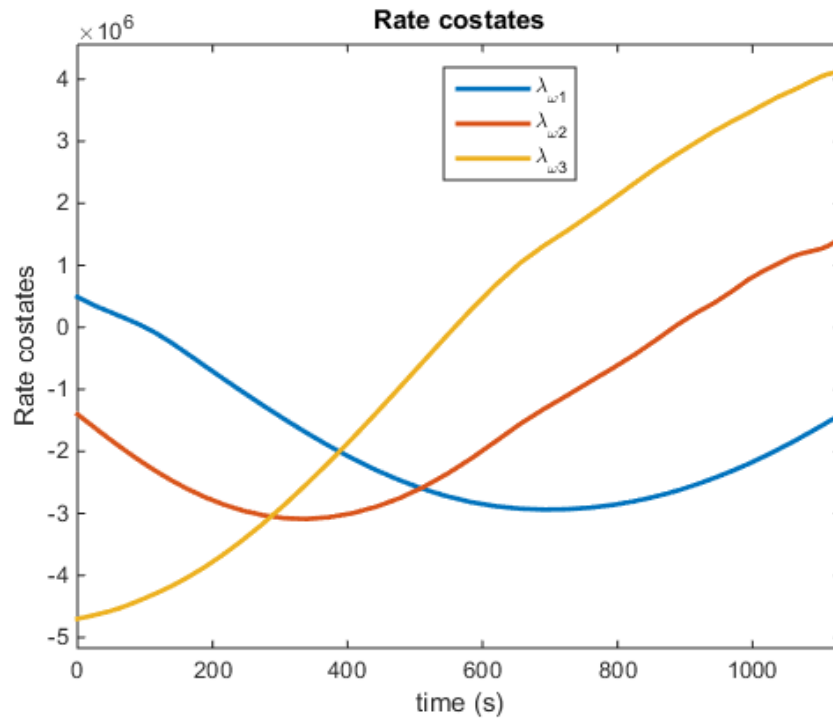


Figure 13. Rate costates for initial problem formulation.

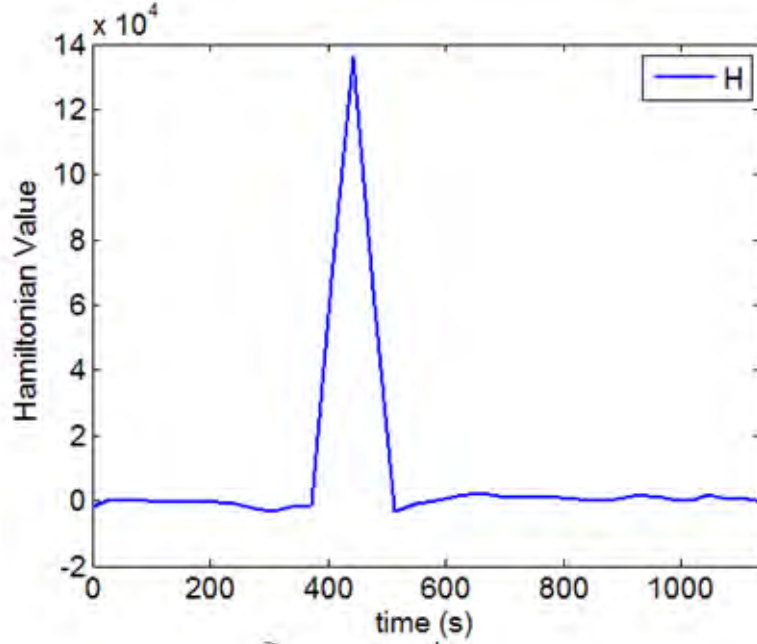


Figure 14. Hamiltonian for the poorly scaled problem formulation.

To resolve this problem, scaling is introduced. When a problem is scaled, the state variables are multiplied by some factor. The idea is to introduce factors such that when the process is followed to calculate and minimize the Hamiltonian and develop the adjoint equation, the equations are affected by changes in variables evenly. That is, scaling is intended to prevent a condition in which a change in a variable is marginalized due to it being orders of magnitude different than other variables.

For initial problem formulation, let the variables  $Q$ ,  $\Omega$ , and  $H$  be scaling factors for the quaternions, angular velocities, and RW momenta, respectively. Then, the scaled variables are

$$\begin{aligned}\bar{x}^T &= [q/Q, \omega/\Omega, h/H] \\ &= [\bar{q}, \bar{\omega}, \bar{h}]\end{aligned}\tag{4.4}$$

By substituting these scaled variables into the optimal control problem and using them to meet the necessary conditions, the magnitude of the costates can

be manipulated. Consider the final term of (4.2), involving the fourth quaternion costate. Substituting (4.4) into this term, we obtain

$$\bar{H} = \dots + \frac{1}{2} \left[ -\lambda_{q_4} \left( \frac{q_1 \omega_1}{Q_1 \Omega_1} + \frac{q_2 \omega_2}{Q_2 \Omega_2} + \frac{q_3 \omega_3}{Q_3 \Omega_3} \right) \right] + \dots \quad (4.5)$$

From (4.5), it is apparent that the order of magnitude of the fourth quaternion costate will vary inversely with several scaling factors for quaternions and angular velocities. Since (4.1) is a minimum time problem, the Hamiltonian must equal negative one throughout the maneuver. By correctly choosing the scaling factors, the problem becomes better scaled such that a small change in the state variable does not cause a large, undesirable change in the costate variables.

The procedure to find the appropriate scaling factors is in some sense a trial and error process. Equation (4.5) represents a relatively simple portion of the Hamiltonian in terms of the relationships of the variables with each other. With many other terms present each affecting one another, it is not possible by inspection to determine how changing the scaling of one variable will affect all of the costates and in turn, the Hamiltonian. The plots of states versus costates provide a starting point to identify disparity in orders of magnitude, but the full effects aren't apparent until the entire process is performed, which in this case is a successful DIDO run. The scaling factors that are used for the problem are shown in Table 4.

Table 4. Scaling factors for initial problem formulation.

Variable	Scaling factor
Quaternions	0.2
Angular velocities	0.003
RW momenta	4.0

The resulting state-costate pairs for angular velocity, as well as Hamiltonian are shown in Figures 15, 16, and 17. The rate state and costate pairs are on the same order of magnitude, which allows for a higher precision solution. The Hamiltonian, while not cleanly a constant negative one, is orders of magnitude closer to the desired value than in the unscaled problem. The scaled simulation completed running in 3,922 seconds, which is roughly a nine-fold improvement over the unscaled case. The results are further explored in Chapter V. It is important to note that the scaling factors are unique to each specific problem, and those in Table 4 are specifically for the conditions discussed in this chapter.

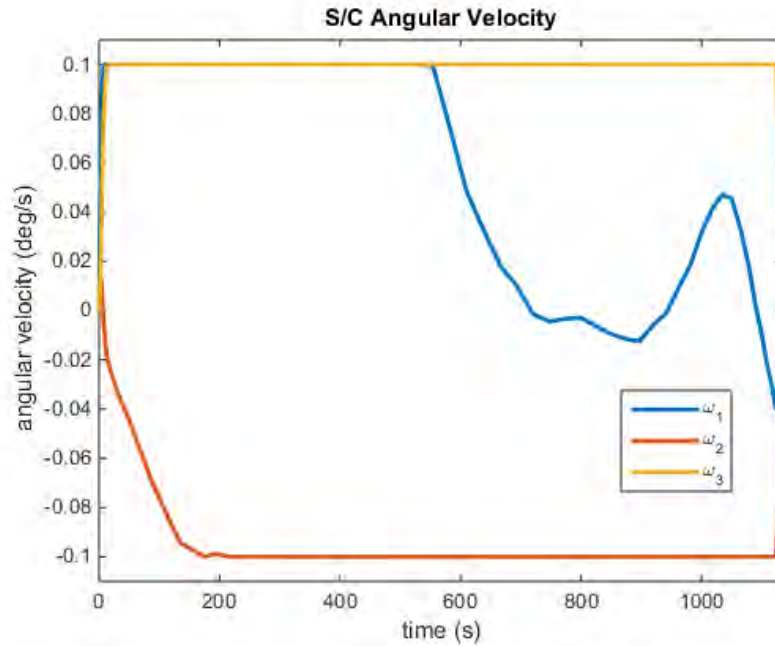


Figure 15. Initial problem formulation: S/C angular velocities for scaled problem.



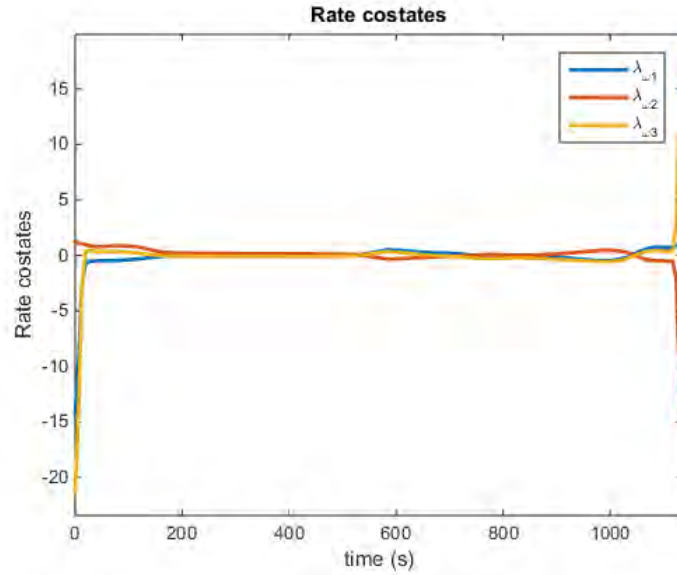


Figure 16. Initial problem formulation: rate costates for scaled problem.

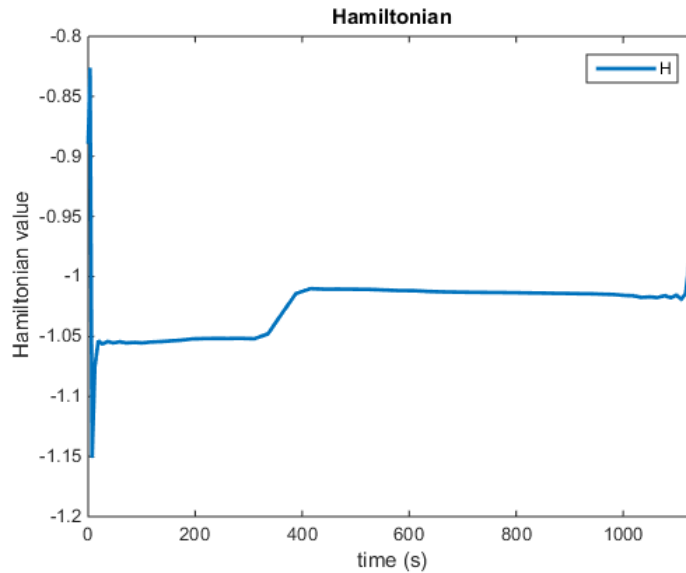


Figure 17. Initial problem formulation: Hamiltonian for scaled problem.

## 2. Angular Velocity Limit

Imposing a limit on angular velocity also causes the developed approach to the optimal control problem to yield subpar results. There are several ways to mitigate this problem. The first is to increase the number of nodes. This would allow more discrete time steps to capture the transients, resulting in a higher

fidelity solution. As discussed, this quickly takes an already impractical time required for calculations and turns it unmanageable, and is not a good path forward. A second approach is to break up the problem into three segments: acceleration, coasting, and deceleration. Continuity of the S/C attitude and velocity as it enters and exits the coasting phase could be presumed using pseudospectral knots [16].

Another mitigation option, and the path chosen for this thesis, is to eliminate the limit on angular velocity, as it is a constraint that is necessary only for conventional slew design. Using the optimal control approach, the limit on angular velocity can be removed since the capacity of the RW assembly should drive the behavior of the system. In doing so, the solution time can be decreased. The angular velocity limit, while necessary for conventional approaches, is not needed for optimal control.

Additionally, a rough calculation was done to find the maximum S/C angular velocity if it were to do a 74 degree slew with a bang-bang control profile, followed by a 128 degree slew. Whether or not the resultant momentum accumulation would violate a RW hardware limit is evaluated. Assuming maximum control torque and zero accumulated RW momentum, equation (2.2) can be used to calculate the following:

$$\begin{aligned}
 \dot{h} &= \tau_{\max} = [0.16, 0.16, 0.16, 0.16]^T \text{ Nm} \\
 \dot{\omega} &= -J^{-1}(\omega \times (J\omega + Zh) + Zh) \\
 \dot{\omega}(0) &= -J^{-1}(\omega_0 \times (J\omega_0 + Zh) + Zh) \\
 &= \begin{bmatrix} -0.0356 \\ -0.000842 \\ 0.000802 \end{bmatrix} \text{ deg/s}^2 \\
 |\dot{\omega}(0)| &= 0.0356 \text{ deg/s}^2
 \end{aligned}$$

Then, this value is used to extrapolate the time it would take to maneuver over the specified angle via a simple double integrator function. This assumes no gyroscopic or damping effects.

$$\theta = \frac{1}{2} \dot{\omega} t^2 \quad (4.6)$$

Equation (4.6) represents the angle rotated through time  $t$  given a constant angular acceleration  $\dot{\omega}$ , assuming the S/C is initially at rest. Thus, to calculate the time to cover a given angle  $\theta$  using a bang-bang control profile, one half of the angle is used to calculate a time for the acceleration, and then the time doubled to account for the deceleration [15]. The maximum S/C angular velocity and RW momentum accumulation can be found by substituting the longest acceleration time into

$$\begin{aligned} \omega_{\max} &= t_{\max} \dot{\omega} \\ h_{\max} &= t_{\max} \tau_{\max} \end{aligned}$$

The fidelity of this calculation is not very high considering it does not take into account the effects of momentum accumulation, nor does it apply to any specific maneuver other than the subtended angle, but it does give a data point to work with.

The resulting maximum S/C angular velocity was 2.1 degrees/sec, which is not an intuitively unreasonable value. The RW accumulated no more than 16 percent of its operational limit in momentum, and the maneuver time is 211 sec. While a very simplified calculation, it does approximate the total amount of time it would take to do a two legged maneuver of appropriate magnitude.

As a result, the rest of this thesis will assume no limit on S/C angular rate, both as an academic exercise and as an exploration on what the LRO is capable of if its wheels are utilized to its design capabilities. Results will be compared against each other and with the simple estimate developed in this section.

THIS PAGE INTENTIONALLY LEFT BLANK

## **V. SUN AVOIDANCE MANEUVERS FOR LRO**

In order to explore the utility of optimal control solutions for LRO maneuver design automation, a variety of different operational scenarios were considered. Specifically, the following conditions were explored:

1. All RW initially have zero stored momentum, such as the state of the S/C immediately after a momentum dump.
2. An initial momentum bias exists, due to accumulated environmental torques.
3. Initial net stored momentum in the body frame is zero, but individual RW have stored momentum due to null redistribution of momentum.
4. Additional pointing constraints introduced to accommodate occultation avoidance of other sensors and instruments

Within conditions two and three, varying magnitudes of initial RW momenta are examined. For condition three, specification (or lack thereof) of final RW momentum values is also examined. Finally, automated maneuver checkout was performed for each of the results using the methods described in Section IV.B. The conditions described above will hereafter be referred to as case 1, case 2, etc.

### **A. CASE 1: ZERO INITIAL MOMENTUM IN ALL WHEELS**

The first condition explored is that of the original problem statement, equation (4.1), as modified per the discussion in Section IV.D. There is no stored momentum in any of the wheels, and thus each wheel has the capacity to store momentum equal in magnitude to its operational limit in either direction. RWs are typically run at some nominal bias rate to avoid friction effects which may corrupt speed measurements. However, these bias rates are typically small enough to be considered zero for practical purposes.

The trajectories of each of the S/C's main axes are shown in Figure 18. The angle that the S/C +z axis makes with the center of the avoidance cone is shown in Figure 19.

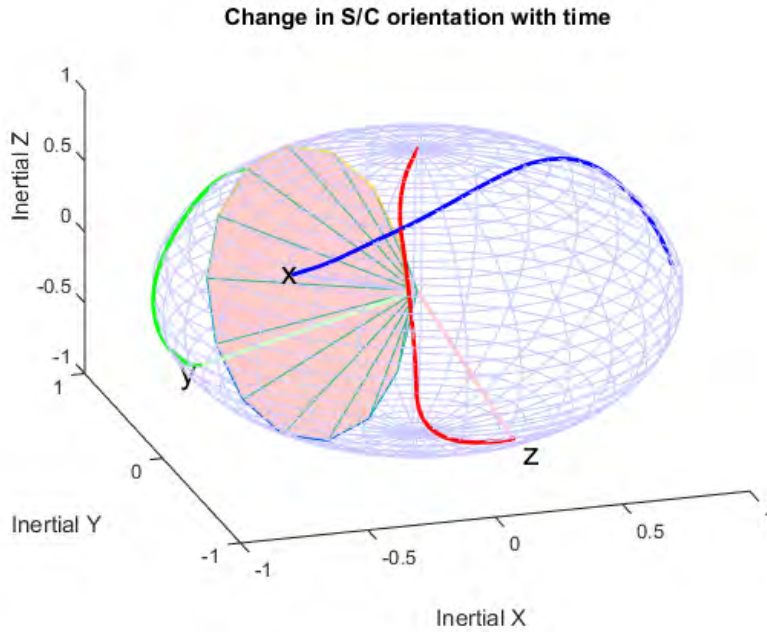


Figure 18. S/C attitude evolution for case 1.

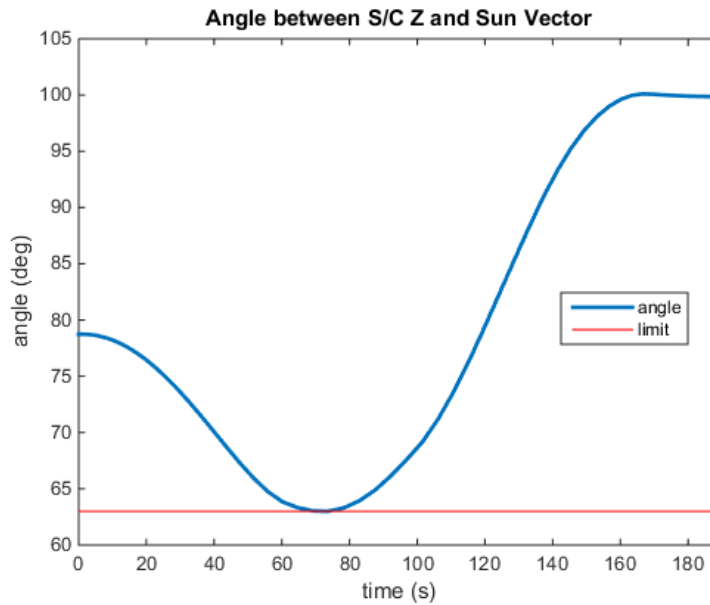


Figure 19. Angle between S/C +z axis and sun vector for case 1.

The paths traced by the S/C axes are smooth curves, indicating a maneuver that is a candidate for implementation. This is in clear contrast with the haphazard appearance of the trajectories obtained using the original unscaled

problem in Figure 7. From Figure 19, it is clear that the maneuver comes as close to the keep out zone as possible without actually violating the constraint. The control signals, S/C angular velocities, and RW momenta follow in Figures 20, 21, and 22.

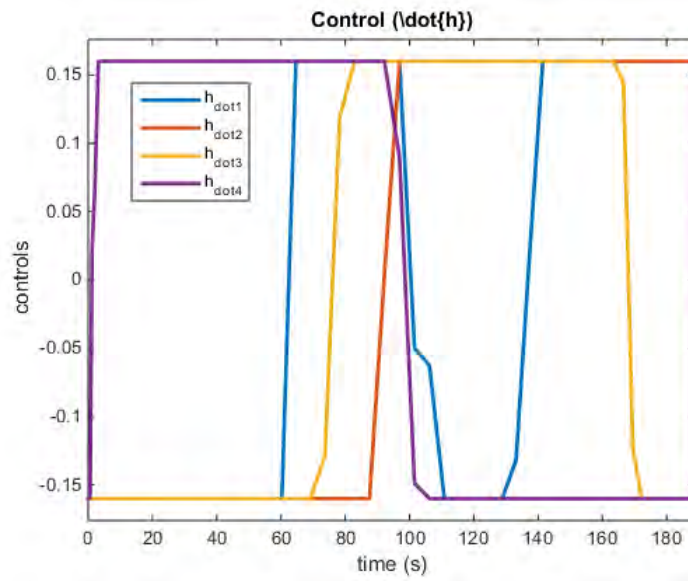


Figure 20. Control signals for case 1.

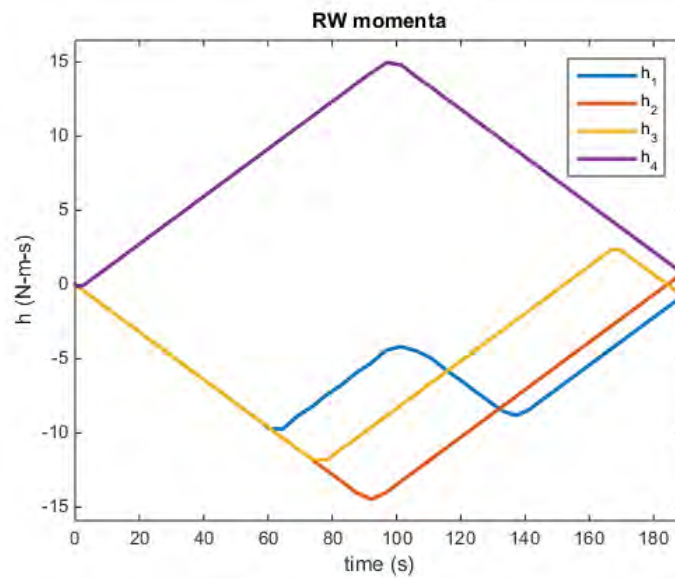


Figure 21. RW momenta for case 1.

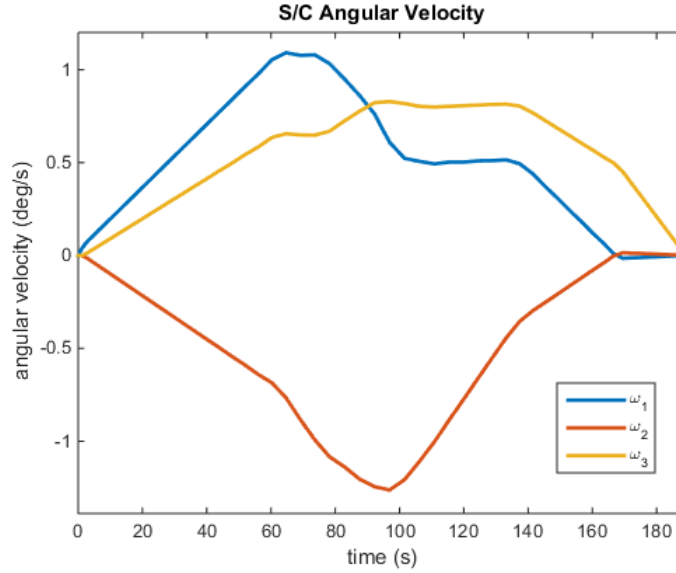


Figure 22. S/C angular rates for case 1.

The control signals are consistent with the bang-bang maneuver expected to be associated with switching functions. The S/C velocity now reaches a maximum of 1.3 deg/s about the y axis, which is 13 times that of the operational limits used on the LRO. However, even though the angular rates are larger than the 0.1 deg/s soft limit, the RW only use about 25 percent of their operational momentum capacity. This confirms the speculation that higher rates are in fact operationally feasible.

The time of the maneuver is 189 seconds. This is a 90 percent improvement over the original, rate limited dogleg maneuver. Compared to the estimate made in Section IV.D.2, it represents a 12 percent improvement. Thus, the optimal control approach succeeds in providing a method for automated maneuver design, while at the same time improving on the maneuver time over the dogleg approach.

### 1. Poor Scaling Example

Another interesting solution that illustrates the need for proper scaling is presented in Figure 23. In this case, the S/C +z axis still successfully avoids the obstacle, as required, but the S/C is seen to rotate in the opposite direction. The



resultant maneuver time is 236 seconds, which is 25% longer than case 1, and 11% longer than the estimated dogleg maneuver time. The solution is a feasible one, and optimal within the numerical fidelity of computation. The Hamiltonian is minimized for this given problem formulation, number of nodes, scaling, etc. This highlights the importance of determining what is proper scaling, as most indications may be that this is indeed an optimal maneuver. In this specific case, there was a disparity in the magnitudes of state costate pairs. This results in a large range of values for a state variable which could have little effect on the Hamiltonian, resulting in a solution that is only locally optimized.

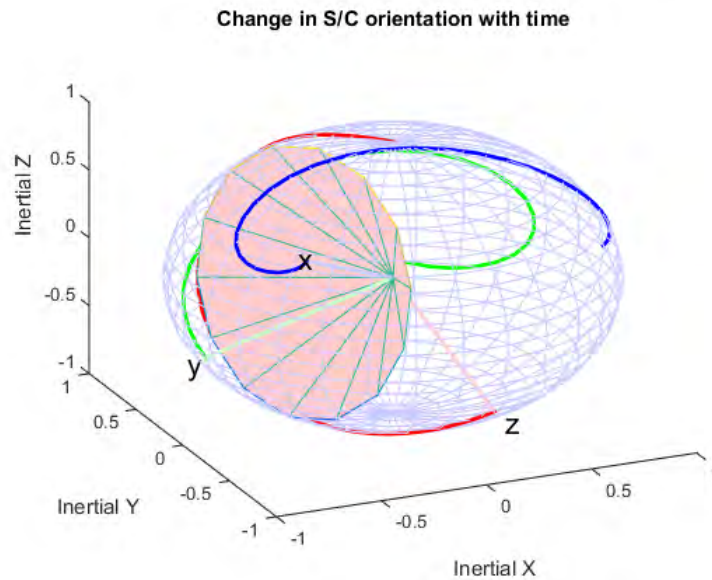


Figure 23. S/C attitude evolution for poorly scaled case 1.

## B. CASE 2: MOMENTUM BIASED CONDITION

Case 2 explores a condition in which all RW are operating at the same speed, in the same direction. This causes a net stored momentum in the S/C body frame, called a momentum bias. Additionally, the initial stored momentum changes the maneuver space in that the RWs are closer to one limit, such as the maximum positive, than the other. If the fraction of the operational momentum limit of the wheel is represented by  $r$ , the initial conditions for the wheels is

written as (5.1). Since RWs can spin in either direction,  $r$  can take on values ranging from negative one to positive one.

$$h_0 = rh_{\max} * [1, 1, 1, 1]^T \quad (5.1)$$

Equation (5.1) is used as part of the specifications of the optimal control problem, which is then solved. The values of  $r$  for which a solution was attempted is summarized in Table 5. Table 5.

Table 5. Summary of initial momentum storage values for case 2.

Case number	$r$
2.1	+0.1
2.2	+0.25
2.3	+0.5
2.4	+0.7
2.5	-0.1
2.6	-0.25

All of the cases contained in Table 5 are solved, and referred hereafter as cases 2.1 through 2.6. In the interest of brevity, not all results will be discussed, but features that distinguish the results will be summarized. Most of the cases essentially build on each other as a confirmation that optimal control can be used to automate the maneuver design process.

The first case of interest is 2.b, where  $r$  is +0.25. This value for  $r$  will also be examined in case 3 and case 4 for continuity. The paths that the S/C's body axes trace out are shown in Figure 24. The angular distance of the +z axis from the center of the obstacle is shown in Figure 25.

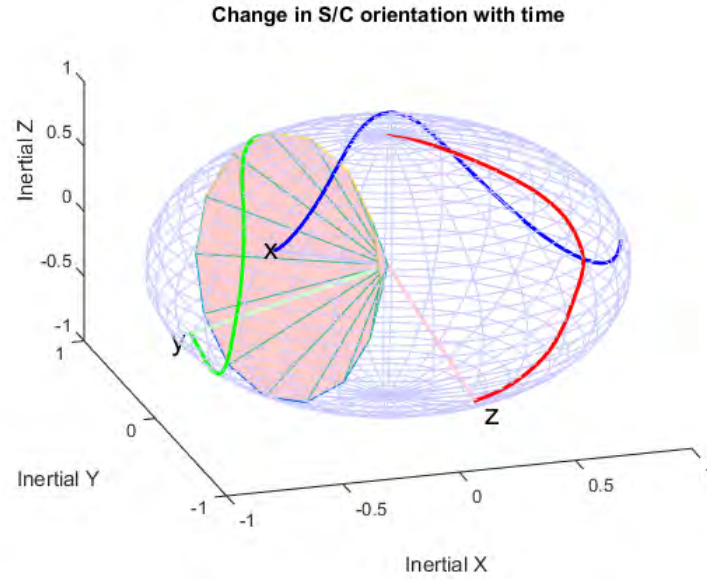


Figure 24. S/C attitude evolution for case 2.2.

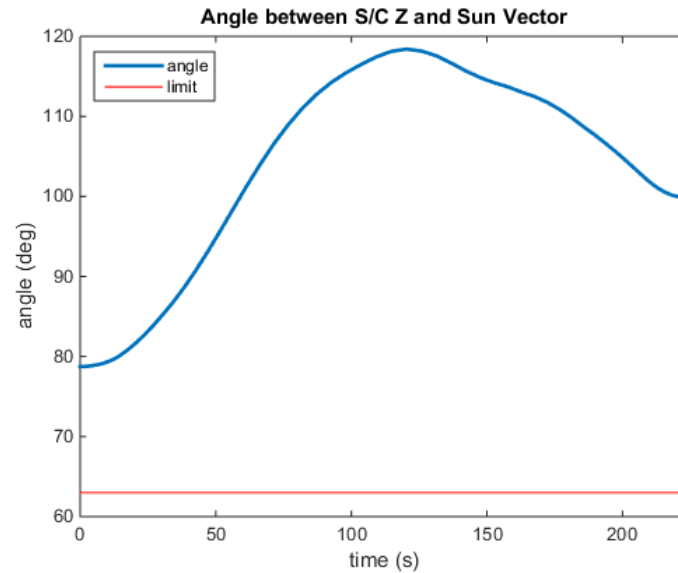


Figure 25. Angle between S/C +z axis and sun vector for case 2.2.

The fact that a momentum bias exists in the system tends to rotate the entire system, and this is evidenced by the spiraling motion of the +x and +y axes. This corresponds roughly to a slow rotation about the +z axis. The effect is due to the fact that as initial momentum bias is increased, the  $\omega \times (J\omega + Zh)$  term in equation (2.2) becomes a larger fraction of the total torque acting on the S/C.

This effect becomes larger as angular velocity and initial momentum bias increase.

Ostensibly, there is some value of  $r$  at which the problem becomes infeasible to solve due to the cross product term dominating the torque, rendering control signals useless at small angular velocities. If dominating is defined to mean that the cross product term is 10 times the magnitude of the control torque when S/C angular velocity is 0.5 deg/s about each axis, then the value of  $r$  which would cause this is only roughly  $\pm 0.17$ , as seen in Figure 26.

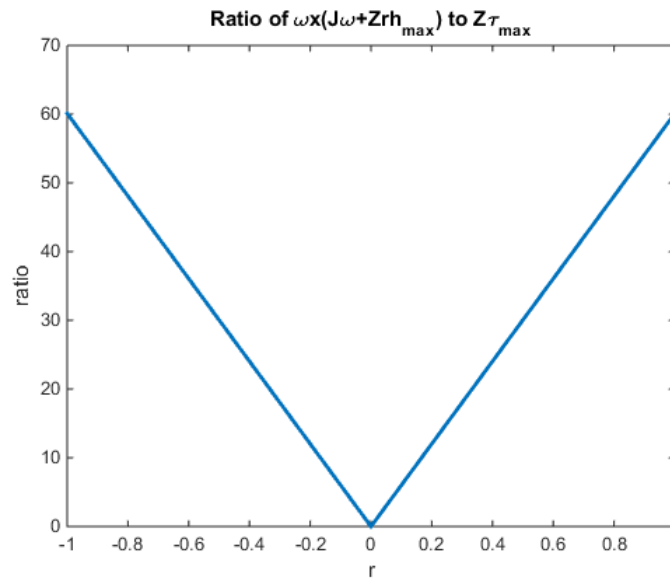


Figure 26. Ratio of  $\omega \times (J\omega + Zrh_{\max})$  to  $Z\tau_{\max}$  as a function of  $r$ , with  $\omega = [0.5, 0.5, 0.5]^T$ .

The S/C angular velocities and momentum storage of each RW are shown in Figures 27 and 28. Compared with case 1, the S/C attains slightly higher velocities. The RW momenta all tend in the same direction, spinning down. This behavior is responsible for the spinning motion of the entire S/C. The solution maneuver time is 224 seconds, which is 18 percent longer than case 1, and six percent longer than the estimated time of the dogleg maneuver.

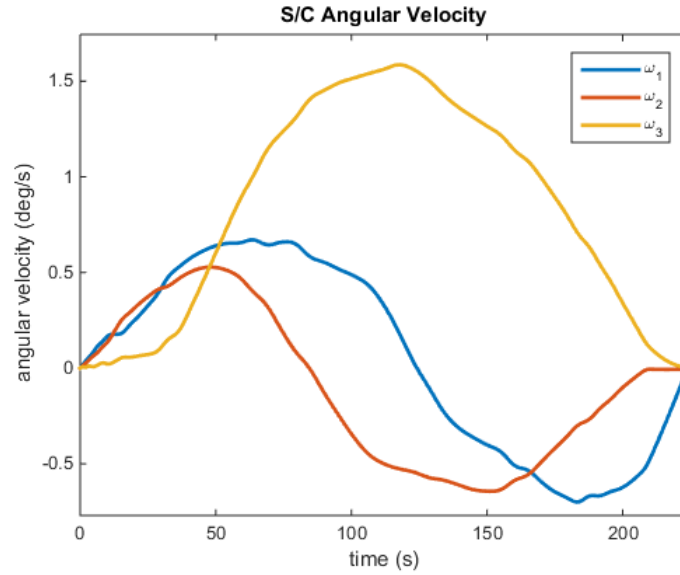


Figure 27. S/C angular rates for case 2.2.

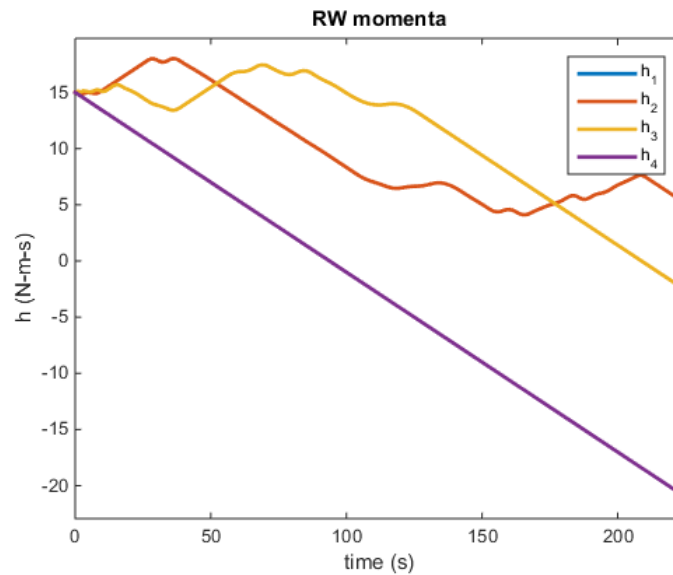


Figure 28. RW momenta for case 2.2.

In case 2.3, where  $r$  is 0.50, the tendency towards spiraling motion becomes far more exaggerated, as seen in Figure 29. Here, the S/C appears to spin almost out of control. However, all boundary and path conditions are satisfied, indicating that control using the RWs is possible despite the large

gyroscopic torques. Therefore, an operational limit on the allowable momentum bias should be specified.

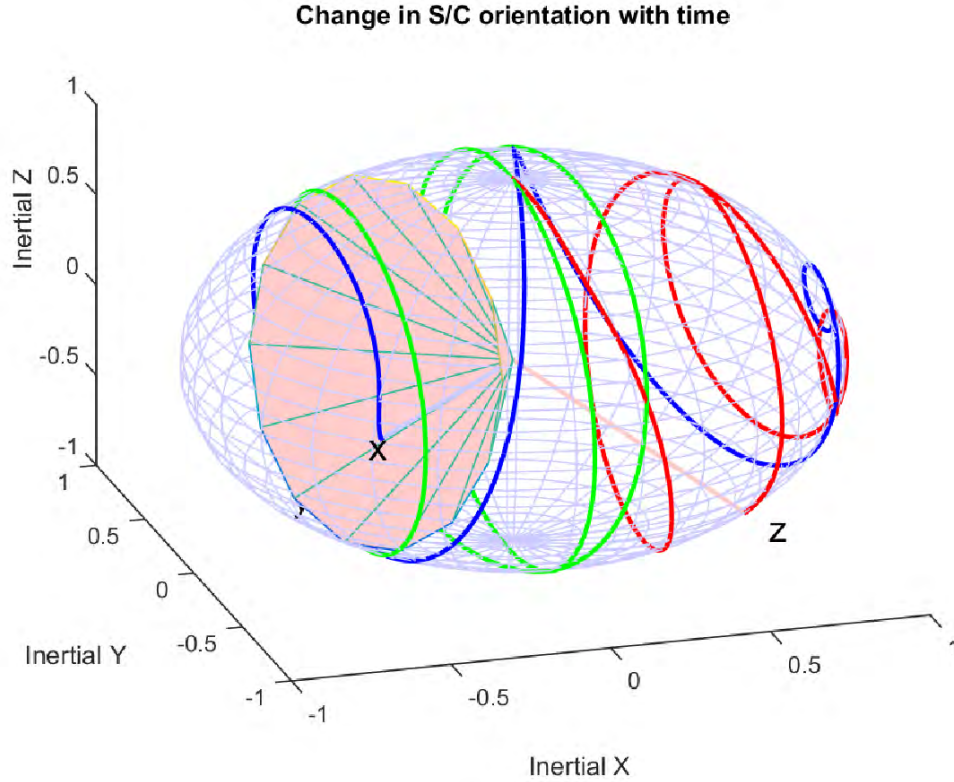


Figure 29. S/C attitude evolution for case 2.3.

### C. CASE 3: ZERO NET MOMENTUM WITH MOMENTUM STORED IN INDIVIDUAL WHEELS

Case 3 involves a zero net momentum condition as with case 1, but this time the RWs will have some accumulated momentum stored in them. It was determined that the zero momentum condition occurs when all wheels are operating at the same speed, with wheels one and three spinning in one direction, and wheels two and four in the other. Using the same notation for fraction of maximum as with (5.1), the initial condition of the wheels can be expressed as

$$h_0 = rh_{\max} * [1, -1, 1, -1]^T \quad (5.2)$$

A summary of the values of  $r$  examined for case 3 is shown in Table 6. Table 6. Those case numbers followed by an “a” denote cases in which a final RW momentum condition was specified.

Table 6. Summary of initial momentum storage values for case 3.

Case numbers	$r$
3.1 and 3.1a	+0.1
3.2 and 3.2a	+0.25
3.3	+0.5
3.4	+1.0
3.5 and 3.5a	-0.1
3.6 and 3.6a	-0.25
3.7	-1.0

#### 1. Case 3 with Final Momentum Unspecified

The solution for S/C attitude motion and standoff angle of the Z-axis from the obstacle are shown in Figures 30 and 31.

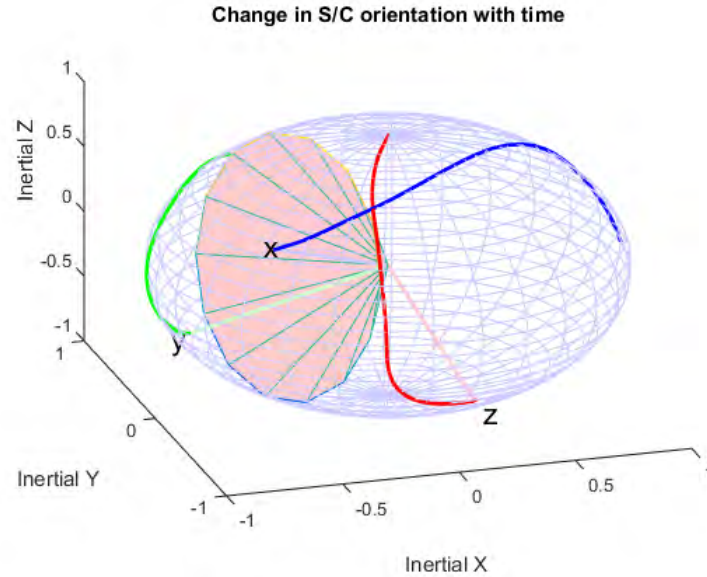


Figure 30. S/C attitude evolution for case 3.2.

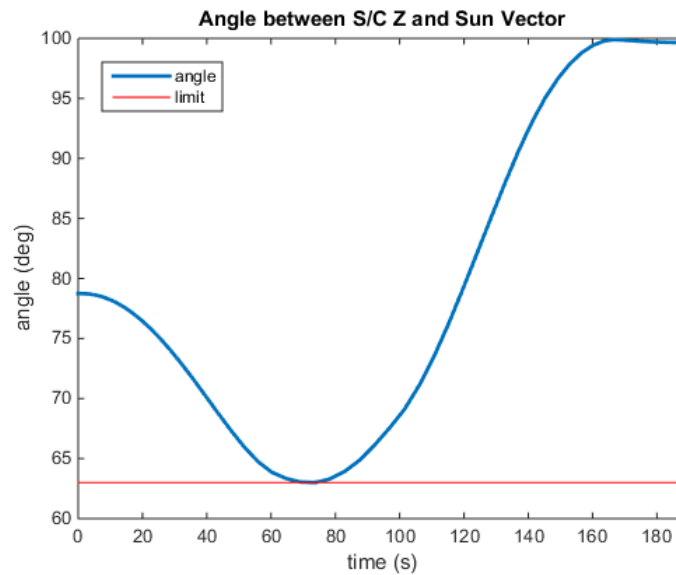


Figure 31. Angle between S/C +z axis and sun vector for case 3.2.

The most important observation is that although the RWs have stored momentum equal in magnitude to case 2.2, the fact there is no net momentum bias allows the solution to evolve similarly to that of case 1. In fact, the differences in the path between case 1 and case 2.2 are so minute that they are not discernable from the figures. The S/C angular velocities and RW momenta,



shown in Figures 32 and 33, tell a similar story. Note that the individual RW momenta in Figure 32 trace the same paths as in Figure 21, but with a bias.

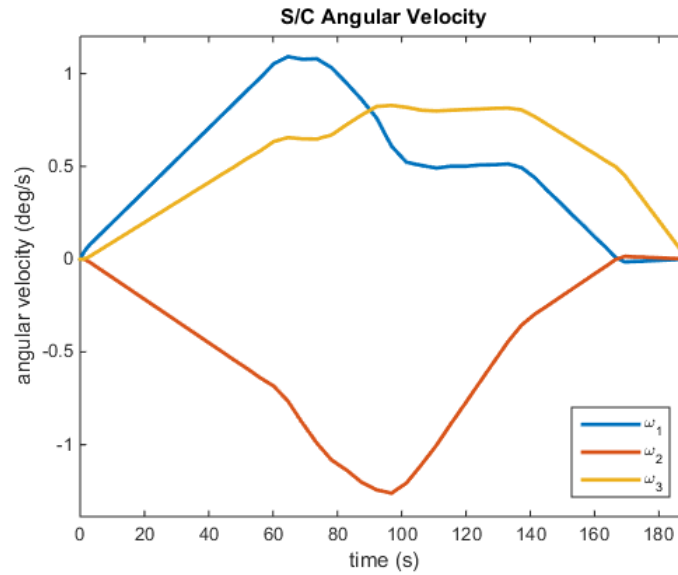


Figure 32. S/C angular rates for case 3.2.

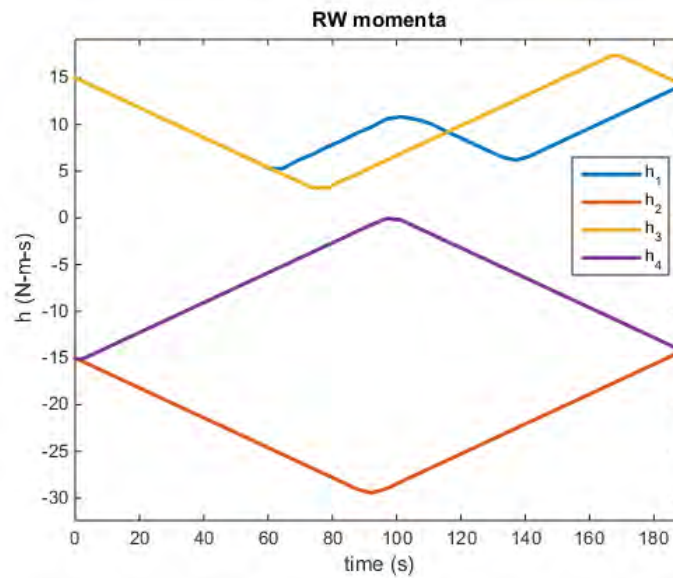


Figure 33. RW momenta for case 3.2.

The solution maneuver time was 189 seconds, which is the same as case 1. Cases 3.1, 3.5, and 3.6 all have solutions very similar to that of case 3.2.

When the magnitude of initial momentum storage in individual wheels is increased to near the wheel capacity, the results change dramatically. Take the extreme example of case 3.7, where the RWs are at their operational limits in terms of momentum storage, but the net momentum in the body frame is still zero. This initial state of the RWs severely restricts the maneuver space of the S/C as the individual wheels cannot spin any faster. The path traced by the body axes and the angular distance of the +z axis from the sun are shown in Figures 34 and 35.

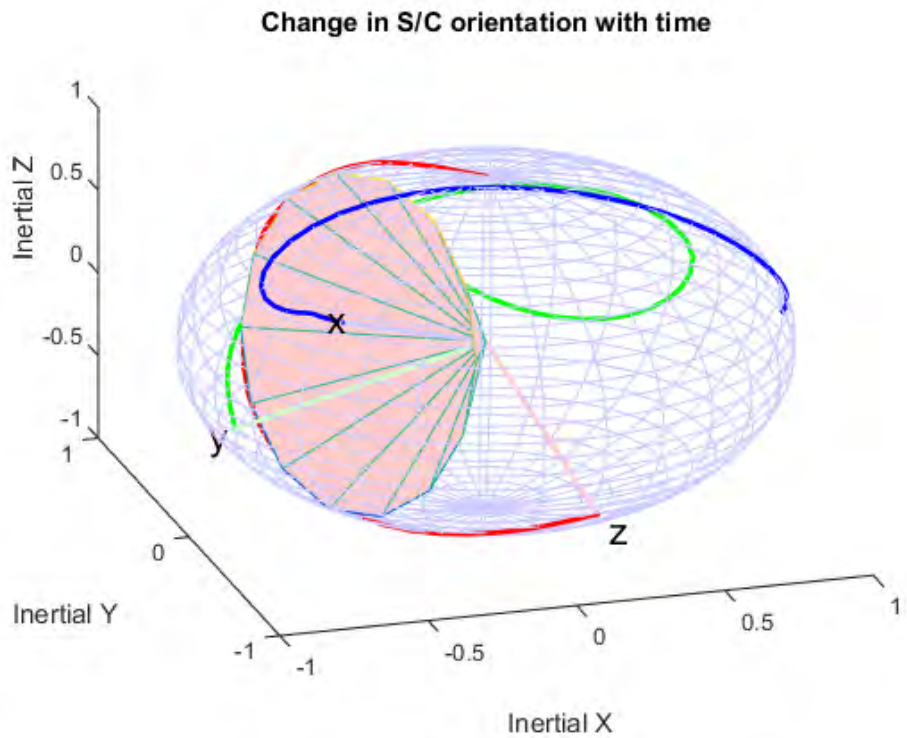


Figure 34. S/C attitude evolution for case 3.7.

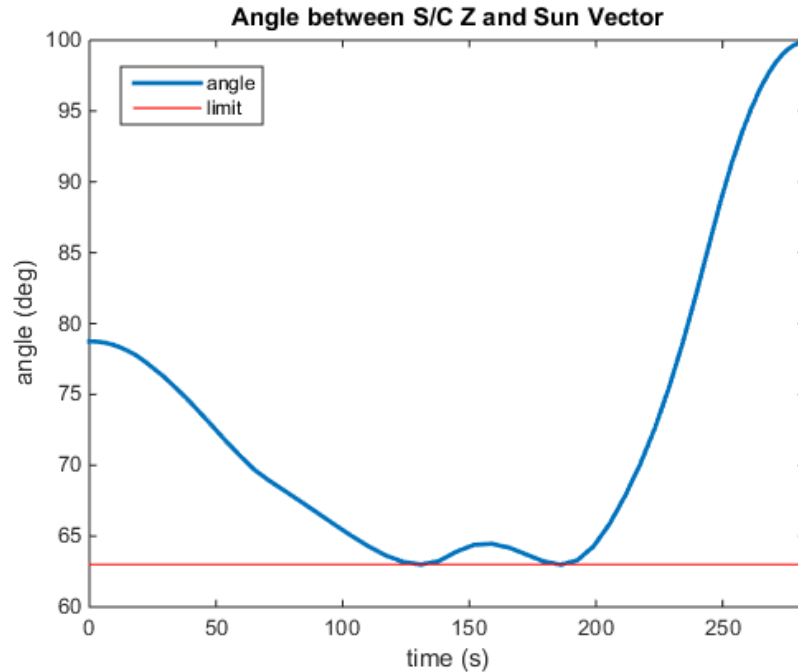


Figure 35. Angle between S/C +z axis and sun vector for case 3.7.

The solution time is 283 seconds, which is 50 percent greater than case 1 and 37 percent greater than the estimated time for the dogleg maneuver. The S/C +z axis traces a path that goes around the obstacle the long way similar to Figure 23, but this time due to the restrictions placed by RW momentum storage. The RW momenta are shown in Figure 36. Note that unlike in Figure 33, not all wheels are being actuated simultaneously at all times due to the operational limitations placed upon them. Case 3.7 proves that a feasible optimal control maneuver could be automatically designed even in a very challenging situation.

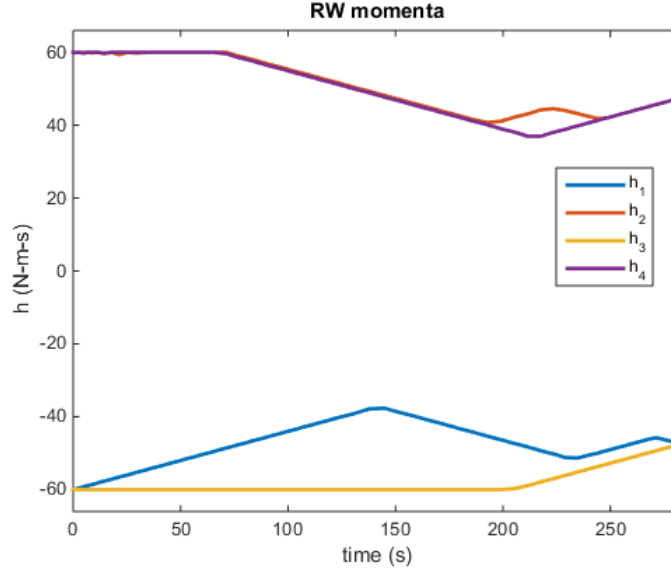


Figure 36. RW momenta for case 3.7.

## 2. Case 3 with Final Momentum Specified

Cases 3.1, 3.2, 3.5, and 3.6 were also solved while enforcing a final boundary condition on the RW momenta. These cases will be referred to as cases 3.1a, 3.2a, 3.5a, and 3.6a. At times, it may be necessary to drive the RWs to a desired state, such as to redistribute stored momentum.

To calculate the final momentum specification, the fact that system momentum is conserved must be used. Since the S/C is stationary at the start and the finish of the maneuver, it follows that all of the system's stored momentum must be entirely in the RW. The momentum stored in the RW expressed in x, y, and z components can be found by left multiplying the RW momentum vector by the  $Z$  matrix. This value must be the same at the beginning and end of the maneuver. Since the S/C orientation changes, the  $Z$  matrix in the inertial frame is not the same at the beginning and end of the maneuver, and thus must be transformed using a DCM. Let  $C$  be the DCM described by (2.4), corresponding to a transformation from  $q = [0, 0, 0, 1]^T$  to a desired quaternion. Then, the desired boundary condition can be found as

$$\begin{aligned}
C_f Z h_f &= C_0 Z h_0 \\
h_f &= Z^\dagger C_f^T C_0 Z h_0
\end{aligned}
\tag{5.3}$$

In (5.3), the dagger denotes the pseudoinverse of the  $Z$  matrix. Since  $Z$  is not a square matrix, it is not invertible. However, a pseudoinverse can be used to solve the equation. The pseudoinverse of  $Z$  is calculated using equation (5.4) where  $Z^*$  is the Hermitian conjugate of  $Z$  [17].

$$Z^\dagger = (Z^* Z)^{-1} Z^* \tag{5.4}$$

Equation (5.3) is imposed as the final boundary condition on RW momentum. This boundary condition also serves as a proof of concept in the ability to despin wheels while performing a maneuver. In this way, momentum redistribution can be performed during a reorientation maneuver. The S/C orientation evolution and angle between +z axis and the obstacle are shown in Figures 37 and 38.

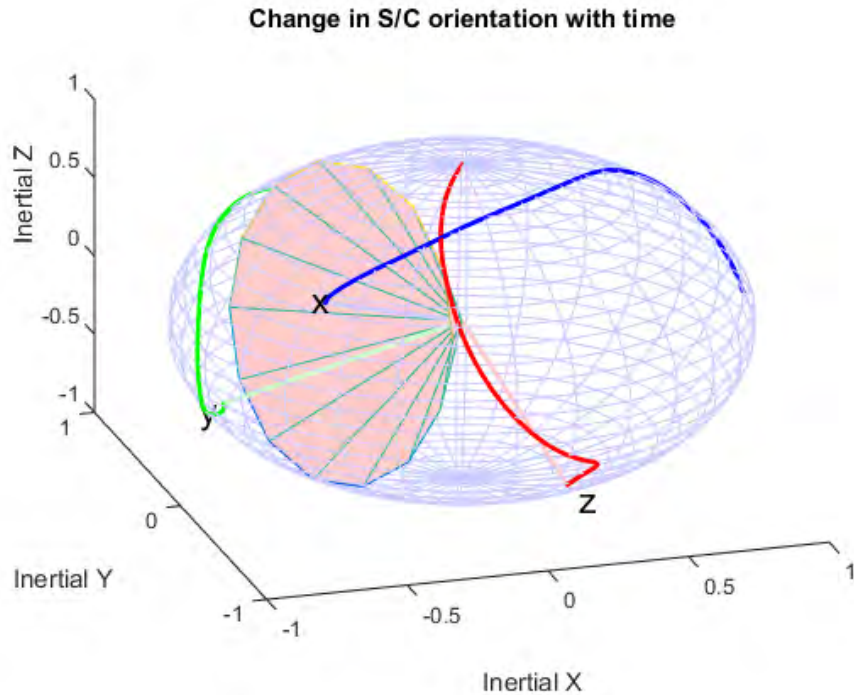


Figure 37. S/C orientation evolution for case 3.2a.

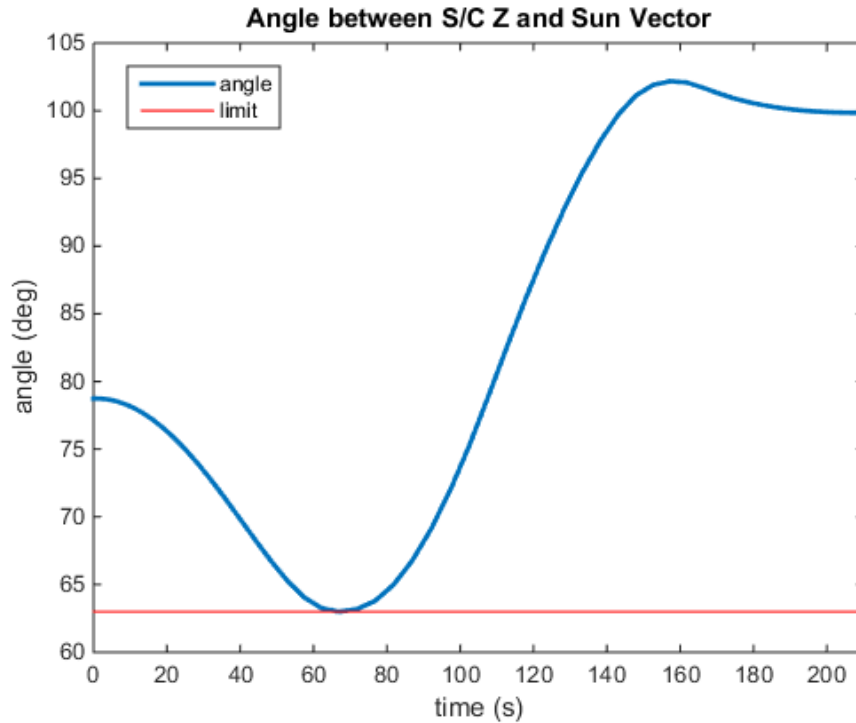


Figure 38. Angle between S/C +z axis and sun vector for case 3.2a.

The paths traced out by S/C axes in Figure 37 are slightly but noticeably different than those in Figures 30 and 31. The maneuver takes 210 seconds, which is 11 percent longer than case 1 and case 3.2, and approximately equal in length to the estimated time for a dogleg maneuver. By forcing the RW to a desired end state, an additional cost is incurred in the form of a longer maneuver, but there may be advantages operationally for increasing this extra cost. The RW momenta are shown in Figure 39. It can be verified that the final condition of the RWs are that they are not spinning, the condition which is consistent with the application of (5.3).

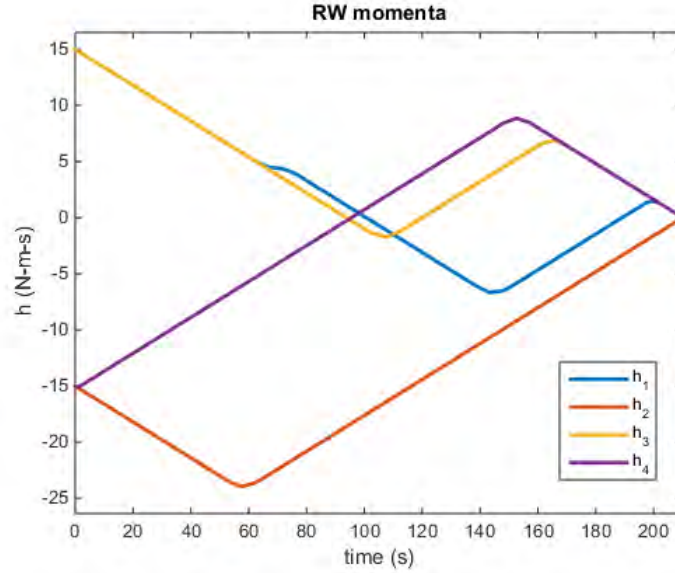


Figure 39. RW momenta for case 3.2a.

#### D. CASE 4: MANEUVERS WITH ADDITIONAL OCCULTATION AVOIDANCE CONSTRAINTS

Cases 1, 2, and 3 explored a maneuver in which there was only one pointing constraint which needs to be satisfied. In reality, as discussed in Table 1, there are multiple constraints for the LRO. To ensure that a maneuver with multiple occultation constraints could be designed, two additional constraints are introduced to the problem formulation. The first additional constraint is a 26.5 degree cone simulating the Earth's disc plus a 15 degree standoff range that the S/C +x axis (simulating the bore sight of a star tracker) must avoid. The second obstacle is a 25.5 degree cone, centered at the sun and therefore oriented in the same direction as the 63 degree cone from previous cases. For this obstacle, the S/C +y axis (another simulated star tracker bore sight) must avoid the cone. The two new pointing constraints that must be added to the optimal control problem formulation are:

$$\begin{aligned}\theta_x &= \cos^{-1}(\hat{E} \cdot \hat{x}) \geq 26.5 \\ \theta_y &= \cos^{-1}(\hat{S} \cdot \hat{y}) \geq 25.5\end{aligned}\tag{5.5}$$

In (5.5),  $\hat{E}$  is the unit vector pointing in the direction of the Earth, and  $\hat{x}$  and  $\hat{y}$  are unit vectors pointing along the S/C +x and +y axes, respectively. These obstacles are placed such that both constraints will be violated by the paths traced in case 3.2, as shown in Figure 40.

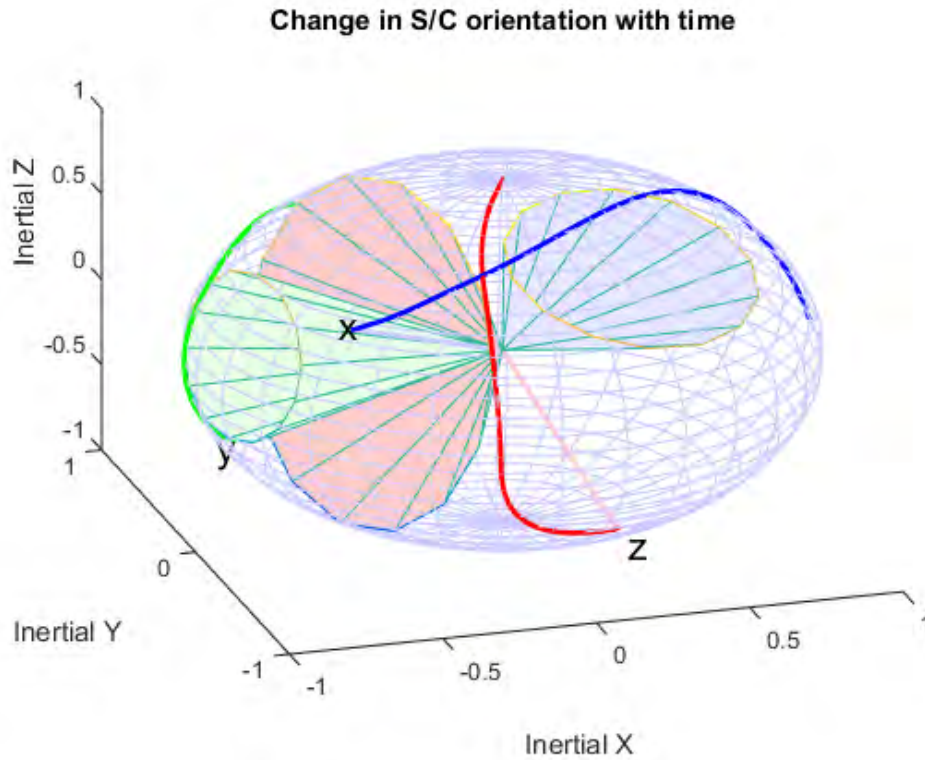


Figure 40. Constraint violations using the path solved for case 3.2.

In Figure 40, the additional keep out cones are colored such that they correspond to the colors of the axis which must avoid the particular cone. The S/C +x axis (blue) clearly violates the blue cone, and the S/C +y axis (green) clearly violates the green cone. The standoff angles of these axes to their respective obstacles are shown in Figures 41 and 42, verifying the pointing violation.



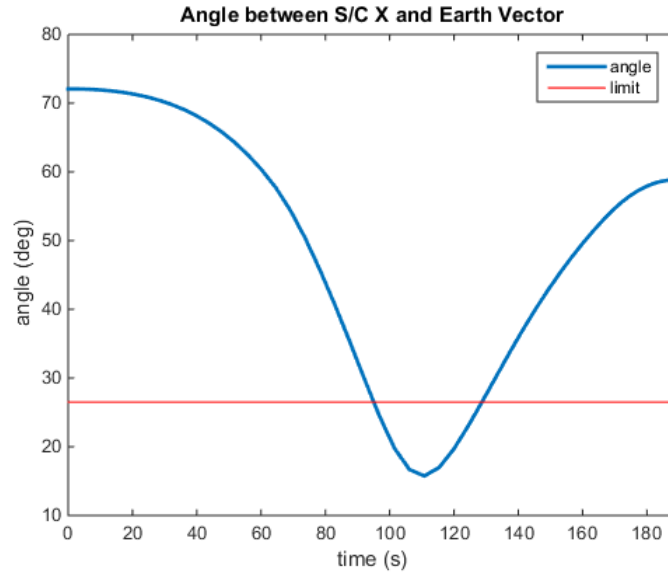


Figure 41. Angle between S/C +x axis and Earth vector for case 3.2.

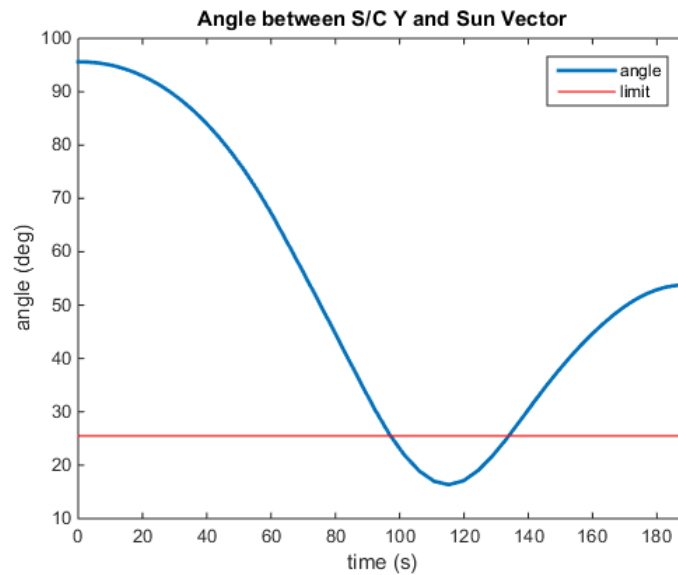


Figure 42. Angle between S/C +y axis and sun vector for case 3.2.

A new maneuver solution was obtained after enforcing the additional occultation constraints. The overall S/C orientation and the angular distances of each axis from their respective obstacles are shown in Figures 43, 44, 45, and 46.

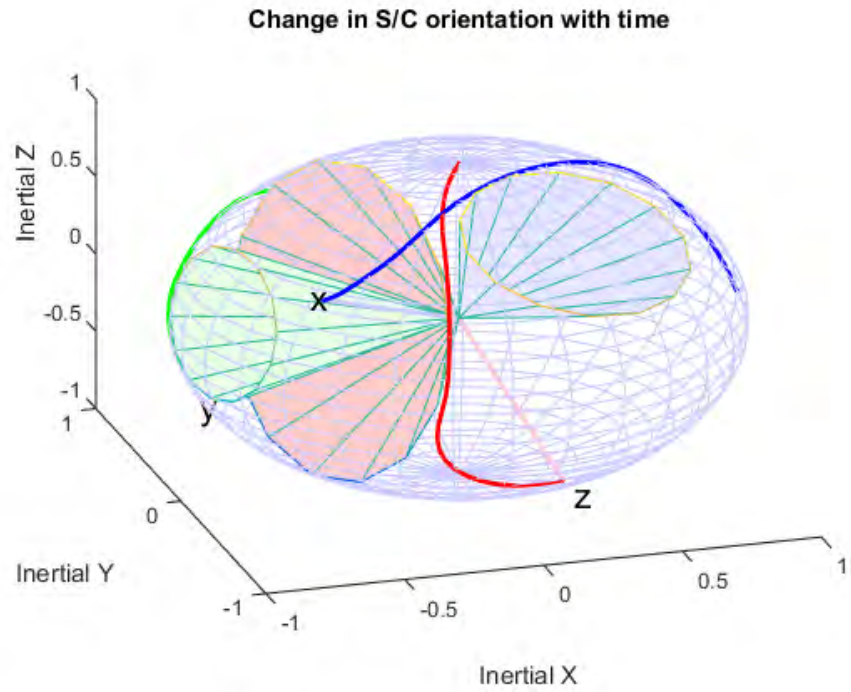


Figure 43. S/C orientation evolution for case 4

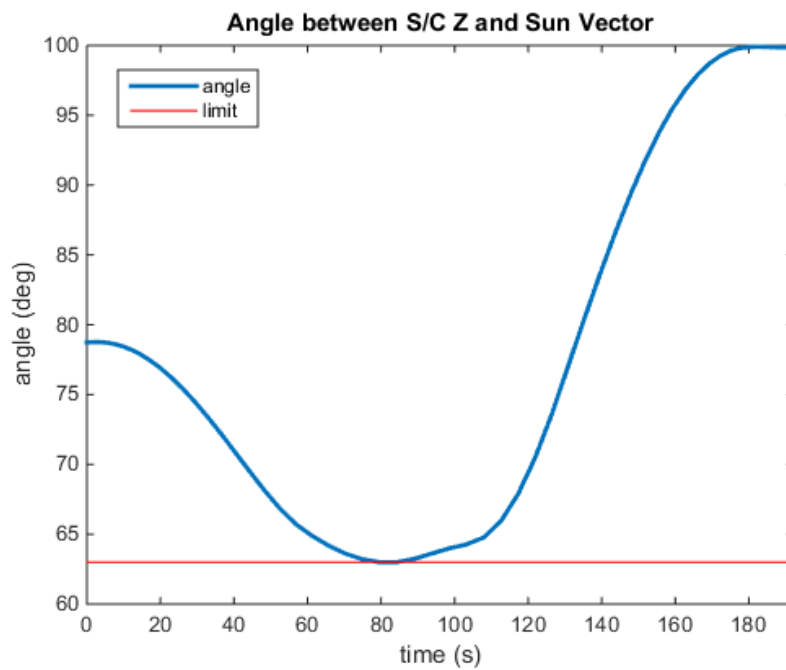


Figure 44. Angle between S/C +z axis and sun vector for case 4

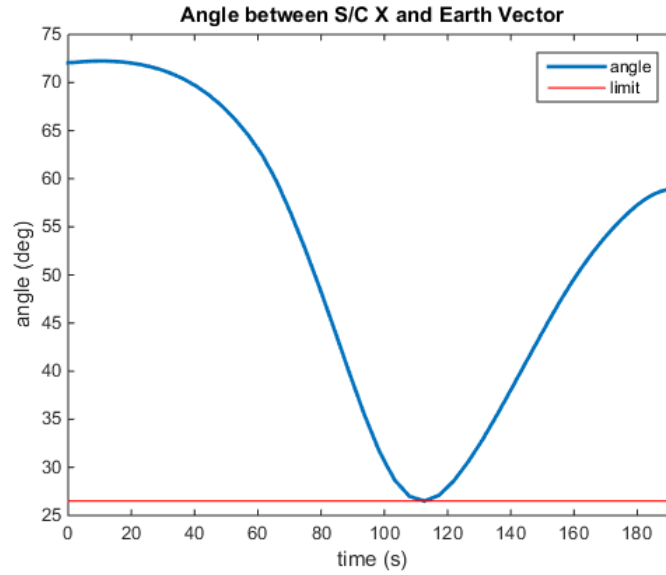


Figure 45. Angle between S/C +x axis and Earth vector for case 4

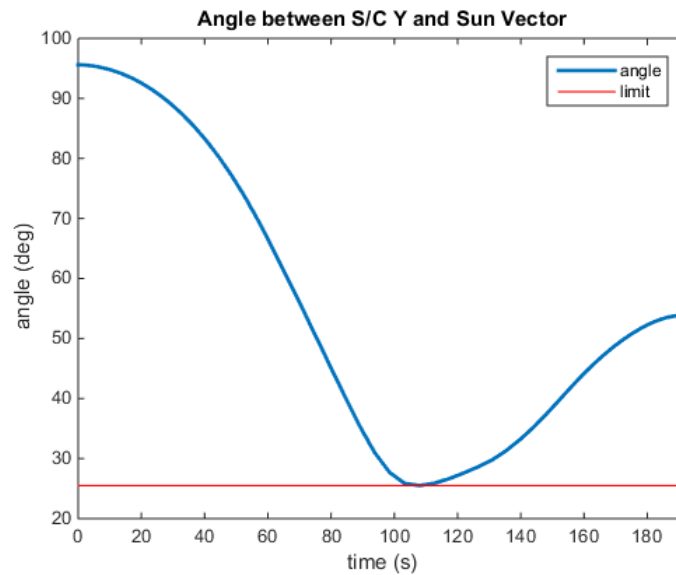


Figure 46. Angle between S/C +y axis and sun vector for case 4

The above figures demonstrate that automated maneuver design is feasible with the introduction of additional occultation constraints. The most remarkable result is that the solution time is 192 seconds, less than two percent longer than case 3.2 with only one obstacle. It is unlikely that this level of performance would be obtained by manually designing a slew as per the

approach outlined in Chapter III. The S/C angular velocities and RW momenta are shown in Figures 47 and 48, illustrating the feasibility of the maneuver.

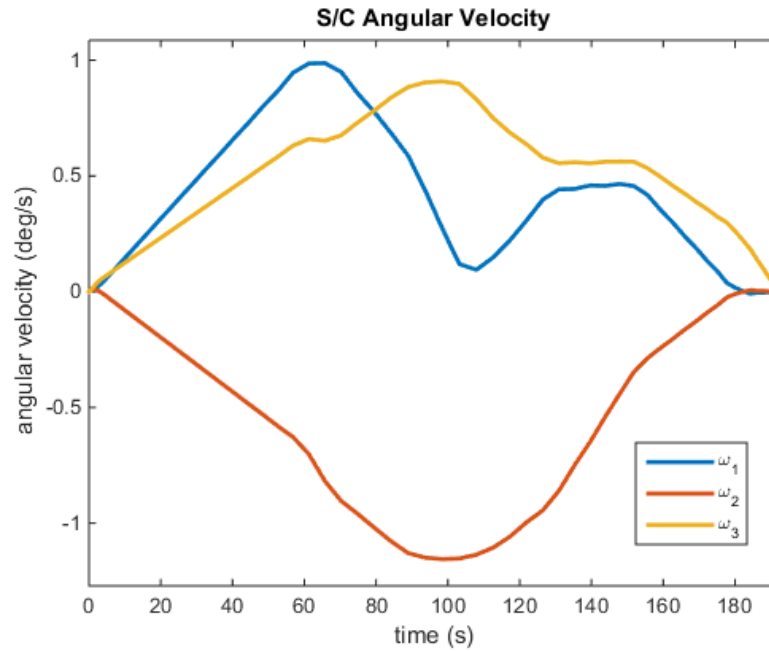


Figure 47. S/C angular velocities for case 4.

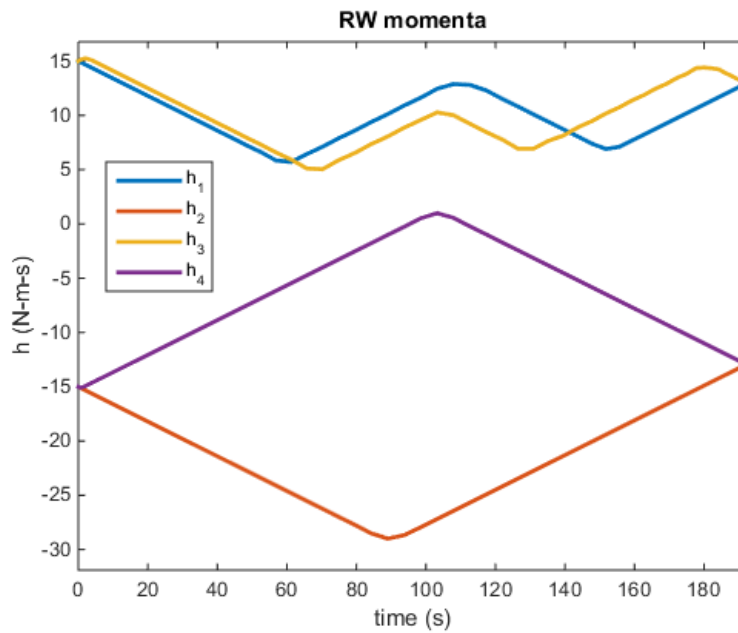


Figure 48. RW momenta for case 4.

## E. MANEUVER CHECKOUT

Maneuver checkout is done in accordance with the methods described in section IV.B. While the checkout steps were performed for all cases, the results for case 4, the most complex case, are presented here.

The first check is to verify that the quaternion norm condition is satisfied throughout the maneuver. The quaternion norm error with respect to time is shown in Figure 49. This condition is clearly satisfied.

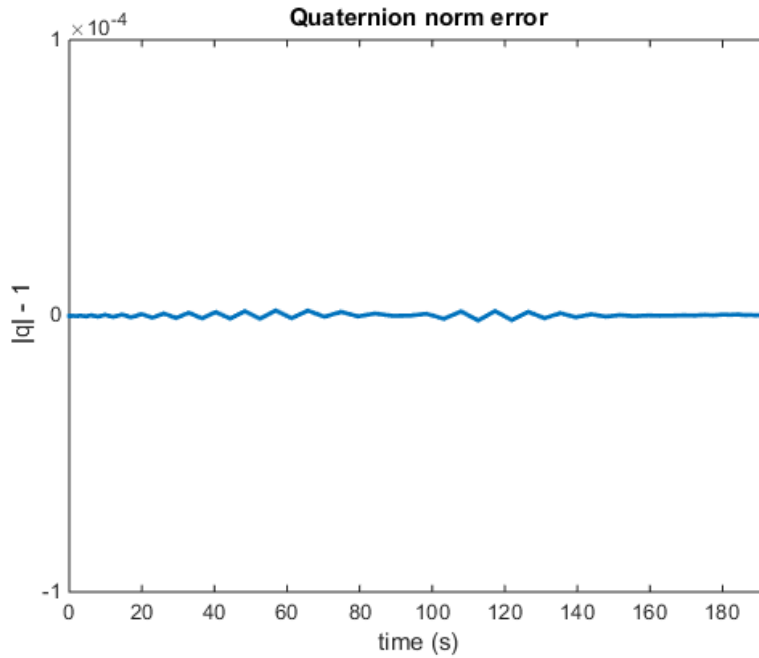


Figure 49. Checkout of the quaternion norm for case 4.

Next, the Hamiltonian is evaluated. For a minimum time maneuver, the Hamiltonian should be a constant at negative one. The Hamiltonian for case 4 is shown in Figure 50. While at first it may appear that the Hamiltonian varies wildly, note the scale. Tiny variations such as those seen in Figure 50 are expected and are due to numerics. The variation of the Hamiltonian is  $4.78 \times 10^{-5}$ . Therefore, it can be concluded that the Hamiltonian value condition is satisfied.

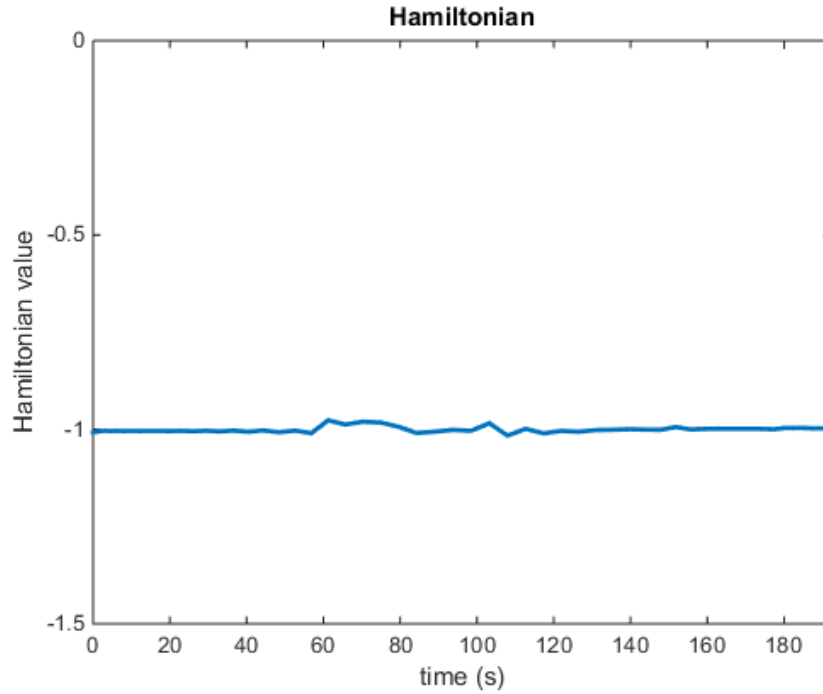


Figure 50. Checkout of the Hamiltonian for case 4.

Additionally, the boundary condition imposed by the transversality condition is verified. For case 4, the momentum costates at the end of the maneuver should be equal to zero. The actual momentum costate functions are plotted in Figure 51. While not exact due to numerics, the momentum costates at the end of the maneuver are close to zero. Thus, the transversality conditions are also satisfied.

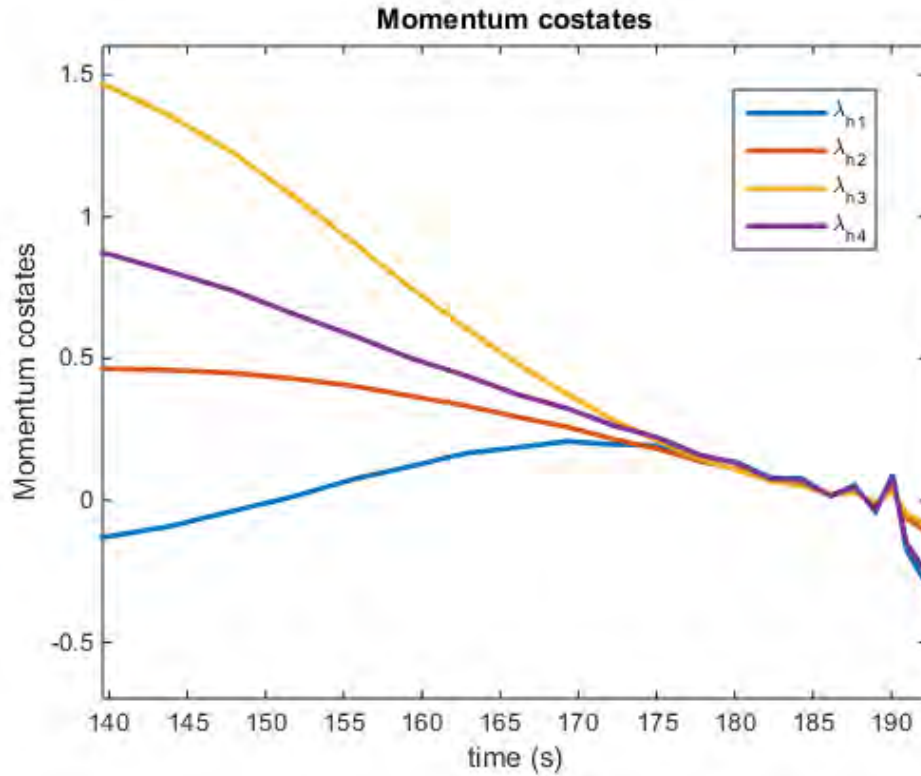


Figure 51. Checkout of the momentum costates for case 4.

Lastly, the control signals are interpolated and propagated using a Simulink propagator. The propagated quaternions, S/C angular velocities, and RW momenta should closely approximate those obtained from DIDO. The propagated results are shown in Figures 52, 53, and 54. The results show that the solution control signals result in the expected S/C behavior. Figure 55 shows the propagated avoidance angle for all three axes.

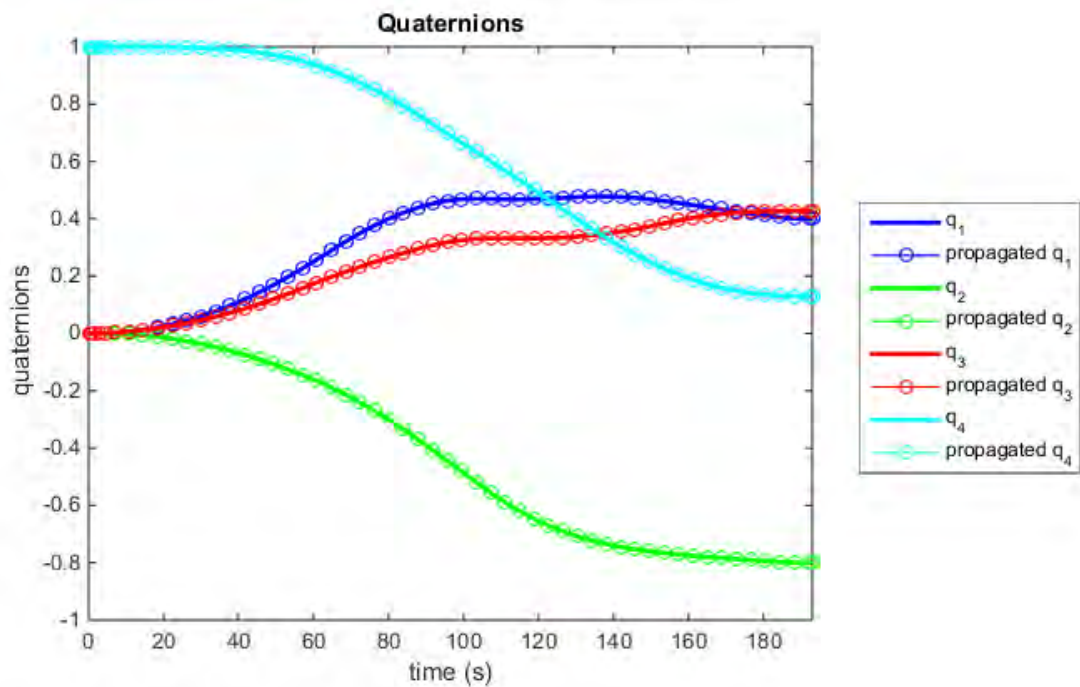


Figure 52. Attitude checkout for case 4.

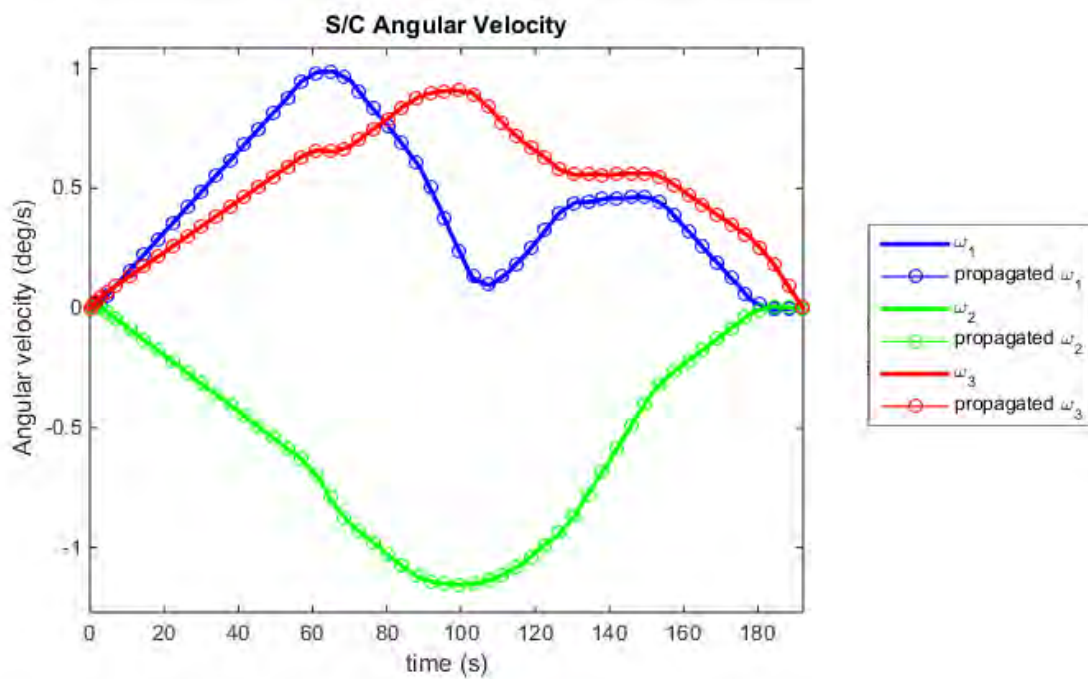


Figure 53. Angular rate checkout for case 4.



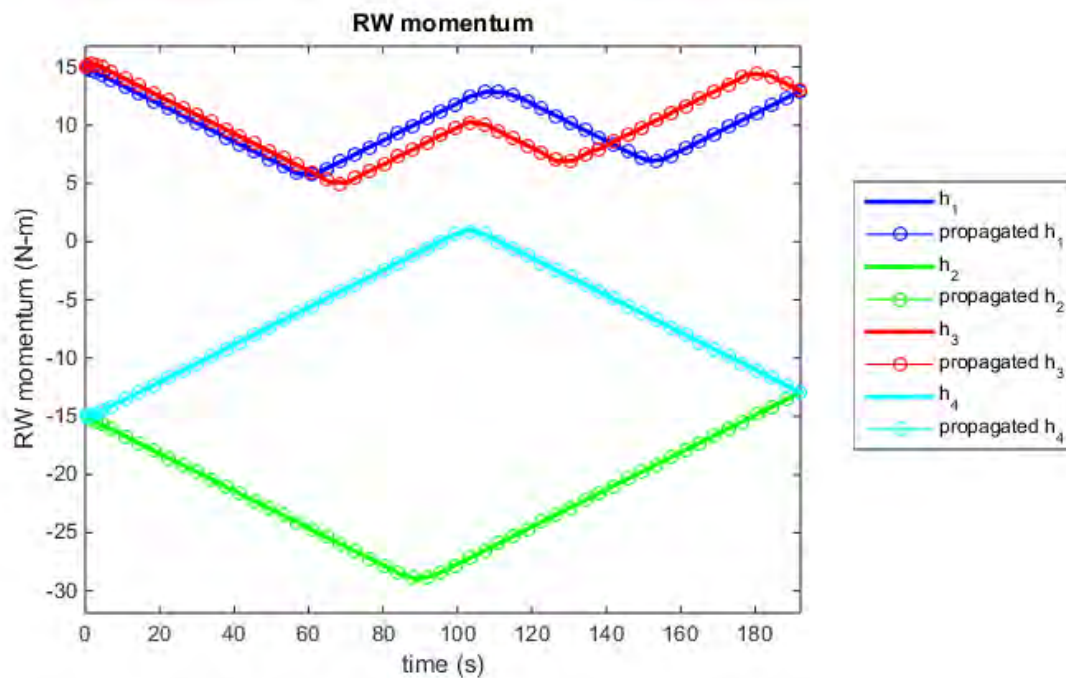


Figure 54. RW momentum checkout for case 4.

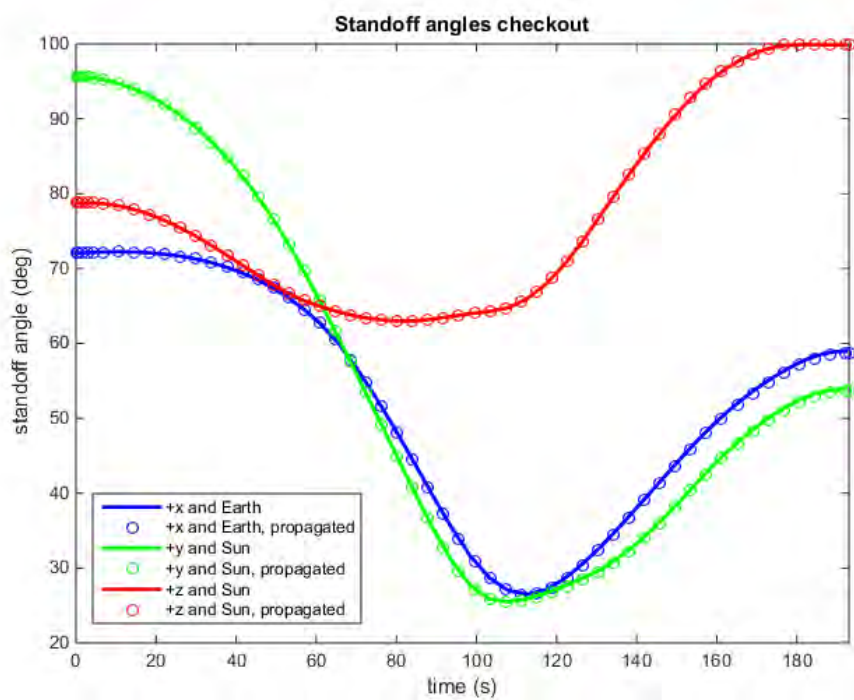


Figure 55. Standoff angles checkout for case 4.

As shown, all checkout exercises for case for were satisfactory. This shows that the maneuver is dynamically feasible and can be implemented in flight. For actual implementation, an approach similar to that used for optimal control implementation on the TRACE S/C can be used [14]. Note also that other constraints, such as thermal constraints can be added as part of the optimal control problem formulation so that the design and checkout process can be automated for these as well.

## **VI. CONCLUSIONS AND FUTURE WORK**

Optimal control theory provides the tools necessary to formulate and solve control problems to optimize control paradigms. The LRO, which uses a manual approach to maneuver design, stands to benefit from automation of maneuver design. To meet the thesis objectives, a slew maneuver was designed such that without intervention, a pointing constraint violation would occur. The LRO would normally use a dogleg maneuver to prevent this pointing constraint violation. When the problem was framed, formulated, and solved as an optimal control problem, reduction in maneuver time of up to 12 percent was realized. If the conventional, rate limited maneuvers are considered, the time savings is up to 90 percent. Additionally, the optimal control approach was able to design maneuvers in challenging conditions, such as an initial momentum bias in the system or the introduction of additional pointing constraints, without human intervention. Optimal control thus provides an automated approach to the design and checkout of maneuvers, simplifying ground segment operations and increasing the potential for science data collection.

Future work can include several topics. One topic is the extension towards automation and prioritization of consecutive maneuvers. It may be that when multiple maneuvers are desired, such as multiple science collects, that there is benefit in considering a specific order for them. Another topic for future work can be to develop an approach to determine an optimal paradigm for momentum dumping, similar to the one demonstrated on the ISS [18]. Such an approach could minimize the number of times momentum dumping occurs, or combine momentum dumping with other slew maneuvers to increase the time utilized for science data collection and/or save on fuel resources.

THIS PAGE INTENTIONALLY LEFT BLANK

## LIST OF REFERENCES

- [1] J. Brill. (n.d.). The LRO Mission. [Online]. Available: <http://lunar.gsfc.nasa.gov/mission.html>. Accessed Nov. 21, 2014.
- [2] R. Garner. (2014, Feb. 4). Lunar Reconnaissance Orbiter. [Online]. Available: [http://www.nasa.gov/mission\\_pages/LRO/spacecraft/index.html#.VHGe9MkntTI](http://www.nasa.gov/mission_pages/LRO/spacecraft/index.html#.VHGe9MkntTI).
- [3] LRO Program Office, private communication, Mar. 2014.
- [4] National Aeronautics and Space Administration, "Spacecraft gravitational torques," NASA LaRC, Hampton, VA, Rep. NASA SP-8024, May 1969.
- [5] J. E. Sedlak and M. B. Houghton, "Lunar Reconnaissance Orbiter (LRO) attitude maneuver planning," presented at the Int. Symp. on Spaceflight Dynamics, Toulouse, France, 2009.
- [6] Goddard Space Flight Center, private communication, Feb. 2014.
- [7] J. Brill. (n.d.). LRO science: Achieving goals. [Online]. Available: <http://lunar.gsfc.nasa.gov/science.html>. Accessed Nov. 21, 2014.
- [8] N. S. Nise, *Control Systems Engineering*, 4th ed. Palo Alto, CA, John Wiley & Sons, 2004, pp. 1–36.
- [9] A. E. Bryson and Y. Ho, *Applied Optimal Control: Optimization, Estimation, and Control*, Revised ed. Boca Raton, FL, CRC Press, 1975, pp. 1–39.
- [10] I. M. Ross, *A Primer on Pontryagin's Principle in Optimal Control*. Carmel, CA: Collegiate Publishers, 2009, Ch 2, pp 19–38.
- [11] F. Fahroo and I. M. Ross, *User's Manual for DIDO 2002: A MATLAB Application Package for Dynamic Optimization*, NPS, Monterey, CA, Tech. Rep., 2002.
- [12] B. Wie, *Space Vehicle Dynamics and Control*, 2nd ed. Ruston, VA: AIAA, 2008, pp. 323–398.
- [13] B. Wie and K. D. Bilimoria, "Time-optimal three-axis reorientation of rigid spacecraft," *J. of Guidance, Control, and Dynamics*, vol. 16, no. 3, pp. 446–452, 1993.

- [14] M. Karpenko *et al.*, “Flight implementation of shortest-time maneuvers for imaging satellites,” *J. of Guidance, Control, and Dynamics*, vol. 37, no. 4, pp. 1069–1079, 2014.
- [15] A. Fleming *et al.*, “Minimum-time reorientation of a rigid body,” *J. of Guidance, Control, and Dynamics*, vol. 33, no. 1, pp. 160–170, 2010.
- [16] F. Fahroo and I. M. Ross, “Pseudospectral knotting methods for solving optimal control problems,” *J. of Guidance, Control, and Dynamics*, vol. 27, no. 3, pp. 397–405, 2004.
- [17] D. Bau III and L. Trefethen, *Numerical Linear Algebra*, Philadelphia, PA: SIAM, 1997, ch. 2, sec. 11, pp. 77–86.
- [18] N. Bedrossian *et al.*, “First ever flight demonstration of zero propellant maneuver attitude control concept,” presented at the AIAA Guidance, Navigation and Control Conf., Hilton Head, SC, 2007.

## **INITIAL DISTRIBUTION LIST**

1. Defense Technical Information Center  
Ft. Belvoir, Virginia
2. Dudley Knox Library  
Naval Postgraduate School  
Monterey, California